Science Advances

11 AUGUST 2023

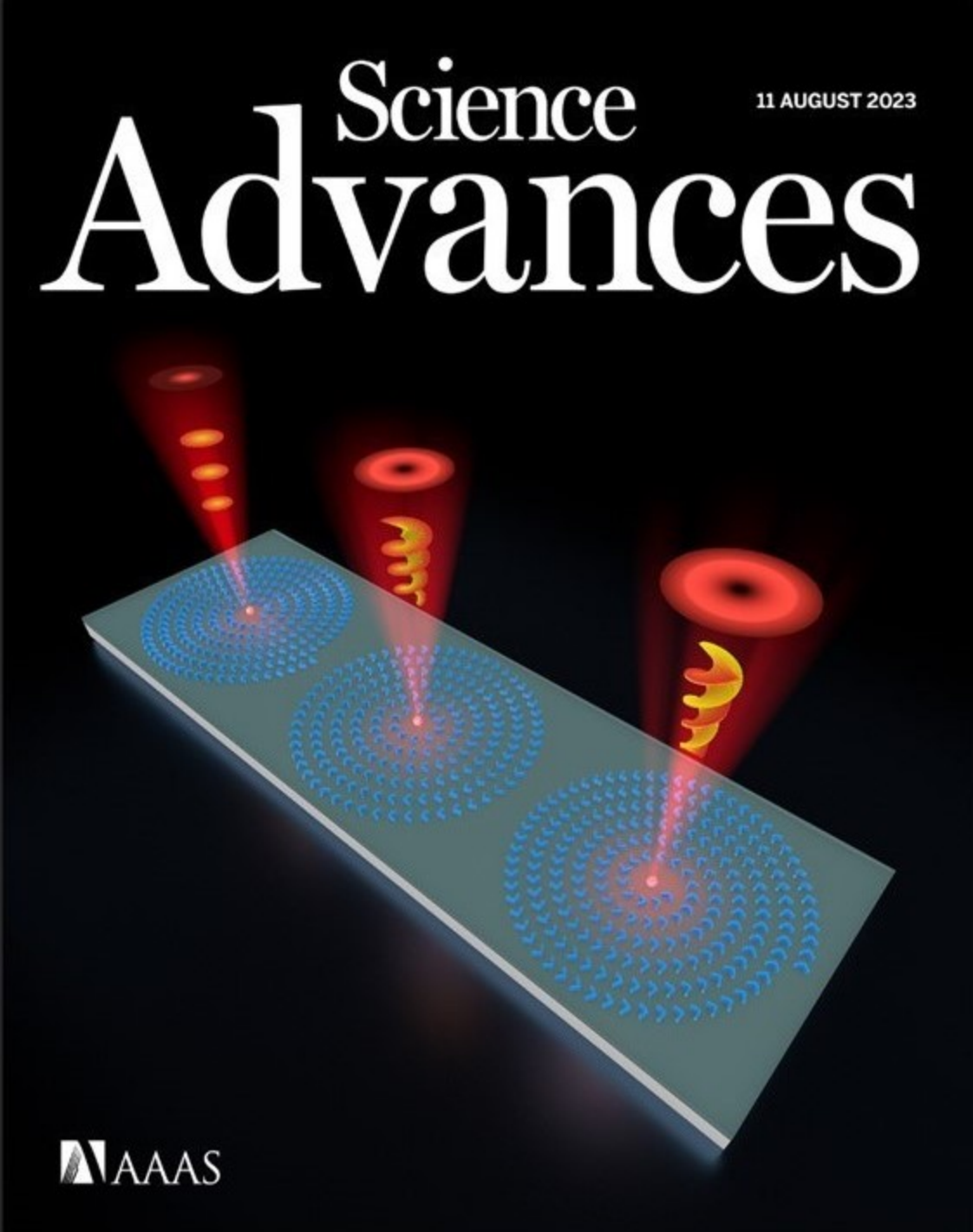

AAAS

PHYSICS

On-chip generation of single-photon circularly polarized single-mode vortex beams

Xujing Liu[1,2]†, Yinhui Kan[2]†, Shailesh Kumar[2], Danylo Komisar[2], Changying Zhao[1], Sergey I. Bozhevolnyi[2]*

Generation of single photons carrying spin and orbital angular momenta (SAM and OAM) opens enticing perspectives for exploiting multiple degrees of freedom for high-dimensional quantum systems. However, on-chip generation of single photons encoded with single-mode SAM-OAM states has been a major challenge. Here, by using carefully designed anisotropic nanodimers fabricated atop a substrate, supporting surface plasmon polariton (SPP) propagation, and accurately positioned around a quantum emitter (QE), we enable nonradiative QE-SPP coupling and the SPP outcoupling into free-space propagating radiation featuring the designed SAM and OAM. We demonstrate on-chip room-temperature generation of well-collimated (divergence < 7.5°) circularly polarized (chirality > 0.97) single-mode vortex beams with different topological charges (ℓ = 0, 1, and 2) and high single-photon purity, $g^{(2)}(0) < 0.15$. The developed approach can straightforwardly be extended to produce multiple, differently polarized, single-mode single-photon radiation channels and enable thereby realization of high-dimensional quantum sources for advanced quantum photonic technologies.

INTRODUCTION

Structuring single-photon emission and engineering photon states triggers breakthroughs in fundamental physics (*1*, *2*) and underpins a broad range of modern quantum technologies (*3*–*6*). One of the forefront research fields is chiral quantum optics making use of unique degrees of freedom associated with photon spin orbital momentum (SAM) (*7*–*9*) and orbital angular momenta (OAM) (*10*–*12*). The superpositions of right- and left-circular SAM states ($|R\rangle$ and $|L\rangle$) and OAM states ($\pm\ell$) encoded in single photons can advantageously be exploited for advanced applications in high-dimensional quantum information processing (*5*, *13*–*16*). Chiral (i.e., SAM encoded) photon emission has been realized at low temperatures by applying a strong magnetic field (*17*, *18*) and then splitting the excitation transitions in specially engineered nanostructures, e.g., a photonic crystal waveguide (*18*). The low-temperature generation of single photons with different SAM-OAM superposition states has also been demonstrated using quantum emitters (QEs) coupled to microring resonators (*19*, *20*). Although the requirement of low-temperature operation restricts eventual practical applications, the reported configurations suggest possibilities for on-chip generation of single photons encoded with SAM-OAM states by coupling QEs with individual nanostructures, an approach that is different from using spontaneous parametric down conversion in bulk nonlinear crystals (*21*, *22*) or external mode transformation (*23*–*25*), all suffering from low photon generation efficiency, low scalability, and complicated transformation process.

Metasurfaces, representing extended surface nanostructures, exhibit unique capabilities for arbitrarily shaping electromagnetic fields, becoming a staple in classical optics (*26*–*31*). Very recently, metasurfaces have been introduced to empower single-photon sources (*32*–*36*), opening thereby design pathways unattainable for configurations that involve QEs coupled to individual nanostructures. The "meta-atom" approach, in which a QE is efficiently and nonradiatively coupled to surface plasmon polariton (SPP) modes that are in turn outcoupled to free-space propagating radiation by QE-encircling dielectric nanoridges (*37*), is especially attractive due to its efficiency (*38*), versatility (*33*, *35*), and the possibility for room-temperature generation of circularly polarized single photons (*37*, *39*). A careful analysis of the underlying physics involved in the photon generation by such a meta-atom revealed a daunting fundamental challenge: Conventional configurations of QE-encircling nanoridges, such as constant-width (*33*, *38*) and width-varying (*37*) concentric nanoridges or Archimedean spiral gratings (*39*), can efficiently generate only radially polarized photons (*35*). Generation of purely circularly right or left polarized (RCP or LCP) photons is impossible with spiral or concentric nanoridges because the SPP outcoupling by these ridges does not change the (radially oriented) SPP polarization. As a result, any spiral or concentric grating would always generate, simultaneously and with equal efficiency, RCP and LCP beams carrying the same total angular momentum (determined by the number of spirals used), i.e., with their OAM (topological charges) being different by two (*35*, *39*). Similar fundamental limitations are also found in other configurations, rendering single-photon generation of single-mode SAM-OAM vortex beams extremely challenging if not impossible (*40*).

In this work, we propose the general approach that enables independent manipulation of the single-photon SAM ($|\Psi\rangle_{SAM}$) and OAM ($|\Psi\rangle_{OAM}$) states by using dimers of orthogonal nanorods (DONRs), generating high-purity $|\Psi\rangle_{SAM}$, arranged in metasurface arrays controlling $|\Psi\rangle_{OAM}$. Using nanodiamonds (NDs) containing nitrogen-vacancy (NV) centers positioned precisely within dielectric DONR-based metasurfaces atop silver (Ag) films, we demonstrate a set of room-temperature on-chip single-photon sources of well-collimated circularly polarized single-mode vortex beams. The DONRs are carefully designed to efficiently convert SPP modes (by outcoupling) to free-space propagating RCP photons with near-

[1]Institute of Engineering Thermophysics, Shanghai Jiao Tong University, Shanghai 200240, China. [2]Centre for Nano Optics, University of Southern Denmark, DK-5230 Odense M, Denmark.
*Corresponding author. Email: seib@mci.sdu.dk
†These authors contributed equally to this work.

perfect purity (98% for $S_3 > 0.9$) and with the negligibly small (<0.3%) spatial overlap between RCP and residual LCP photons. Furthermore, by arranging the DONRs along different (spiral and concentric) trajectories, high-purity SAM states are superimposed with OAM states corresponding to different phase-front helicities (topological charges): ℓ = 0, 1, and 2. The generated single-photon RCP single-mode vortex beams exhibit a low divergence (< 7.5°) and robust characteristics with respect to small QE misalignments (±50 nm).

RESULTS

Design of on-chip SAM-OAM photon sources

The general design concept is based on devising individual nanostructures that would outcouple (radially polarized) SPP waves into circularly polarized free-space propagating radiation and aligning these nanostructures along trajectories chosen according to the desired OAM. One could opt for resonant plasmonic (metal) nanorods, whose perpendicular dipole moments scatter with the $\pi/2$ phase difference (*41*, *42*), but the inevitable photon absorption by metal nanorods would jeopardize the single-photon generation efficiency. We suggest using instead pairs of orthogonal dielectric nanorods, i.e., DONRs, whose separation along the SPP propagation ensures the proper phase difference between their main dipole moments. Following this concept, we place ND-NVs on a Ag substrate covered by a silica (SiO_2) spacer and arrange the designed DONRs made of hydrogen silsesquioxane (HSQ) along the OAM-corresponding trajectories (Fig. 1A). Note that the ND-NVs are considered being excited with a tightly focused radially polarized laser beam (not shown in Fig. 1A), an excitation that favors vertical electric dipoles exciting cylindrically diverging SPP waves propagating along the multilayer substrate surface (*37*–*39*, *43*).

In general, the polarization of the photon emission outcoupled from QE-excited SPPs by a DONR can be represented as the SAM superposition state in the circularly polarized basis ($|R\rangle$ and $|L\rangle$) (*44*)

$$|\Psi\rangle_{\mathrm{SAM}} = C_1|R\rangle + C_2|L\rangle \quad (1)$$

with C_1 being unequal to C_2 due to scattering anisotropy, unlike the case of outcoupling with nanoridges (*39*). Arranging metasurface DONRs (oriented identically with respect to radially diverging SPP wave) along spiral trajectories separated by the SPP wavelength in the radial direction results in the corresponding OAM superposition states as follows (*39*)

$$|\Psi\rangle_{\mathrm{SUP}} = C_1|R\rangle|l_R = m+1\rangle + C_2|L\rangle|l_L = m-1\rangle \quad (2)$$

Table 1. Three arrangements (M1, M2, and M3) for different SAM-OAM single-photon states generated by QE-coupled quantum metasurfaces.

Metasurfaces arrangement	$\|\Psi\rangle_{\mathrm{OAM}}$	$\|\Psi\rangle_{\mathrm{SAM}}$
M1: Diverging spiral trajectory	$\|\ell = 0\rangle$	$\|R\rangle$
M2: Concentric trajectory	$\|\ell = 1\rangle$	$\|R\rangle$
M3: Converging spiral trajectory	$\|\ell = 2\rangle$	$\|R\rangle$

Here, m is the number of spiral arms with $m < 0$ for counterclockwise spirals. In our approach, we first design an individual DONR to obtain a high purity SAM state $|\Psi\rangle_{\mathrm{SAM}}$ (e.g., with $C_1 \to 1$ and $C_2 \to 0$) and then arrange the DONR elements along the spiral trajectories to ensure the generation of a desirable OAM state superimposed with a given SAM state. For example, by outcoupling QE-excited SPPs with azimuthally arranged DONRs, each producing the RCP photons, along diverging (counterclockwise) spiral, concentric, and converging (clockwise) spiral trajectories, RCP vortex beams with correspondingly different OAMs—l_R = 0, 1, and 2—are generated (Fig. 1A).

The individual DONR represents a pair of orthogonal dielectric nanorods equally inclined (i.e., having ±45°) with respect to the SPP propagation direction (Fig. 1B). In a qualitative treatment (note S1), the QE-excited SPP wave propagating along the x axis is outcoupled by the DONR having the nanorod separation $d = \lambda_{\mathrm{spp}}/4$ into the RCP (LCP) radiation produced by dipole moments generated along the long (short) sides of the nanorods (fig. S1), with the former being the main contribution. The suppression of the unwanted LCP contribution can be very close to total for nanorods with large aspect [length-to-width (l/w)] ratios. Thereby, the generation of high-purity RCP photon emission with $C_1 \to 1$ and $C_2 \to 0$ is feasible, resulting in turn in the generation of the pure superposition state, having a desired OAM (Eq. 2). Likewise, a high-purity LCP superposition state, i.e., with $C_1 \to 0$ and $C_2 \to 1$, can be generated with the DONR mirrored with respect to the x axis (fig. S1).

Nanofabrication of DONRs and the corresponding limitations on the nanorod dimensions, especially on the height-to-width ratio, h/w, result in relatively large nanorod dimensions as compared to the radiation wavelength. Consequently, the nanorods can no longer be treated within the electrostatic approximation and disregarding the interparticle near-field coupling, as implicitly assumed in the qualitative treatment (note S1). Carefully conducted numerical simulations (Materials and Methods) confirmed that the suppression of the unwanted LCP contribution, $I_{\mathrm{RCP}}/I_{\mathrm{LCP}}$, can indeed be close to total, reaching 85, with the Stokes parameter S_3 attaining 0.98 for a slightly larger than expected (from the qualitative treatment) nanorod separation $d = 3\lambda_{\mathrm{spp}}/8$ (Fig. 1C). The simulated performance of the plane SPP outcoupling by a rectangular DONR array with the optimized nanorod separation demonstrates an efficient SPP outcoupling into a well-collimated pure RCP photon beam (Fig. 1D). This excellent performance of an outcoupling DONR array, efficiently performing the SPP-to-circular polarization transformation, has further been verified in the experiment with SPPs being excited by a periodic nanoridge grating illuminated with free-space laser light at 670 nm (note S2 and fig. S2).

With the designed DONR at hand, it is straightforward to devise DONR location trajectories that would efficiently convert radially polarized and cylindrically diverging (QE-excited) SPP waves into circularly polarized photon emission, generating a desirable OAM state superimposed with the SAM state determined by the DONR orientation, i.e., generating a single-mode SAM-OAM encoded vortex beam (Eq. 2 and note S1). The azimuthal arrangements with different spiral trajectories for the generation of three different SAM-OAM states of single photons are schematically shown in Fig. 1A and described in Table 1. The correspondingly designed configurations are displayed in Fig. 2A with the color representing the SPP propagation phase variation (note S1).

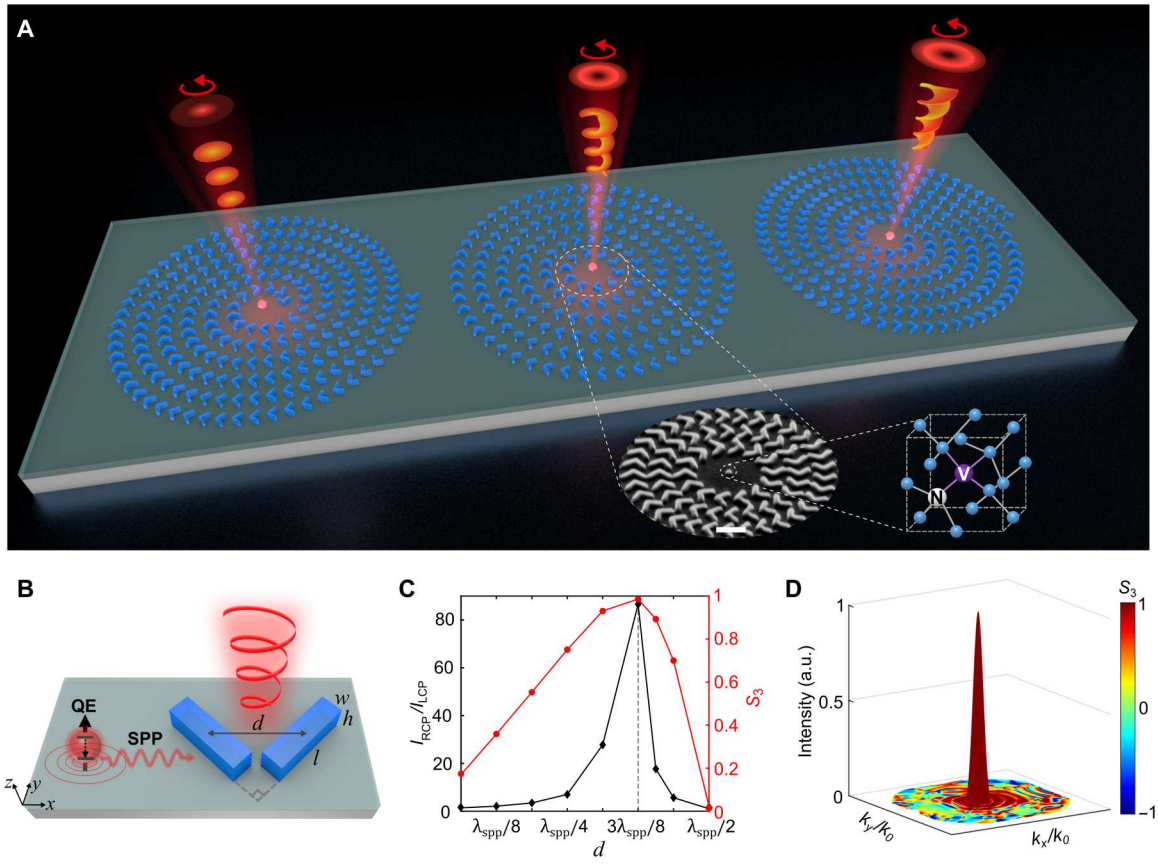

Fig. 1. Design of QE-coupled metasurfaces for SAM-OAM photon emission. (**A**) Schematic of QE-coupled metasurfaces generating single-mode SAM-OAM photon emission with different topological charges: l_R = 0, 1, and 2. The ND-NVs are surrounded by DONRs aligned along the OAM-corresponding trajectories. Insets: Angular view scanning electron microscopy (SEM) image of the central part of the fabricated metasurface along with the ND-NV schematic. Scale bar, 500 nm. (**B**) Illustration of SAM generation by DONR outcoupling of the QE-excited SPP wave. An individual DONR consists of two orthogonal nanorods with the width (*w*) = 100 nm, length (*l*) = 400 nm, and height (*h*) = 150 nm. (**C**) Intensity ratio of RCP and LCP components (left axis) and Stokes parameter S_3 (right axis) as a function of the nanorod separation *d* calculated at the radiation wavelength of 670 nm by considering the outcoupling of a plane SPP wave incident on a rectangular (7 μm by 6 μm) periodic array composed of DONRs. (**D**) Three-dimensional (3D) representation of the superimposed far-field intensity and polarization distribution of the outcoupled beam produced by the rectangular DONR array with the optimized in (C) nanorod separation. The color indicates the value of Stokes parameter S_3. a.u., arbitrary units.

SAM-OAM generation

We first confirm that the RCP states dominate the photon emission for all three configurations (Fig. 2B) as expected from the qualitative considerations above. The spatial overlaps of the RCP and LCP intensity distributions are found to be negligibly small—0.3, 1.7, and 6.7%, respectively—much smaller than those obtained previously with the QE-coupled metasurfaces consisting of continuous nanorods (*37*, *39*). At the same time, the conservation of the total angular momentum noted previously (*35*, *39*) is manifested also with these DONR metasurfaces. For example, the diverging (counterclockwise) spiral results in the dominant RCP radiation concentrated in the far field within a collimated bright spot with the uniform phase distribution, signifying the topological charge $\ell = 0$, while the LCP radiation (weaker by two orders of magnitude) is distributed in a doughnut shape with the phase distribution featuring a singularity with the topological charge $\ell = -2$ (Fig. 2B). Contrary to that, the converging (clockwise) spiral results in the strong RCP radiation shaped as a doughnut, carrying the topological charge $\ell = +2$, while the weak LCP radiation is concentrated within a phase homogenous spot with the topological charge $\ell = 0$ (Fig. 2B).

The RCP relative contribution (weight) can be defined as the ratio of the emission into the RCP radiation, i.e., that with a sufficiently large Stokes parameter $S_3 > \xi$ (ξ is the chiral threshold), to the total emitted power, and it can be estimated from the far-field intensity distribution as follows: $f = \frac{\sum_i I(S_3(i)>\xi)}{\sum_i I(i)}$. For the considered configurations, the RCP weight is rather high (>80%) even when requiring $S_3 > 0.9$, with the largest value of 98.2% found for the RCP generation with the diverging spiral trajectory while being somewhat lower for the concentric and converging spiral trajectories (Fig. 2C). The enhancement of RCP emission as compared with the QE emission without metasurfaces, when calculated as a function of the numerical aperture (NA) of the collecting radiation objective, emphasizes strong collimation of the RCP emission, exceeding three orders of magnitude for NA = 0.1(Fig. 2D).

We have verified the underlying physics of conversion from cylindrically diverging SPP waves into different SAM-OAM states with different DONR trajectories by using an ideal DONR consisting of two orthogonal electric dipoles with the π/2 phase difference to compose the same spiral arrangements. All dipoles are

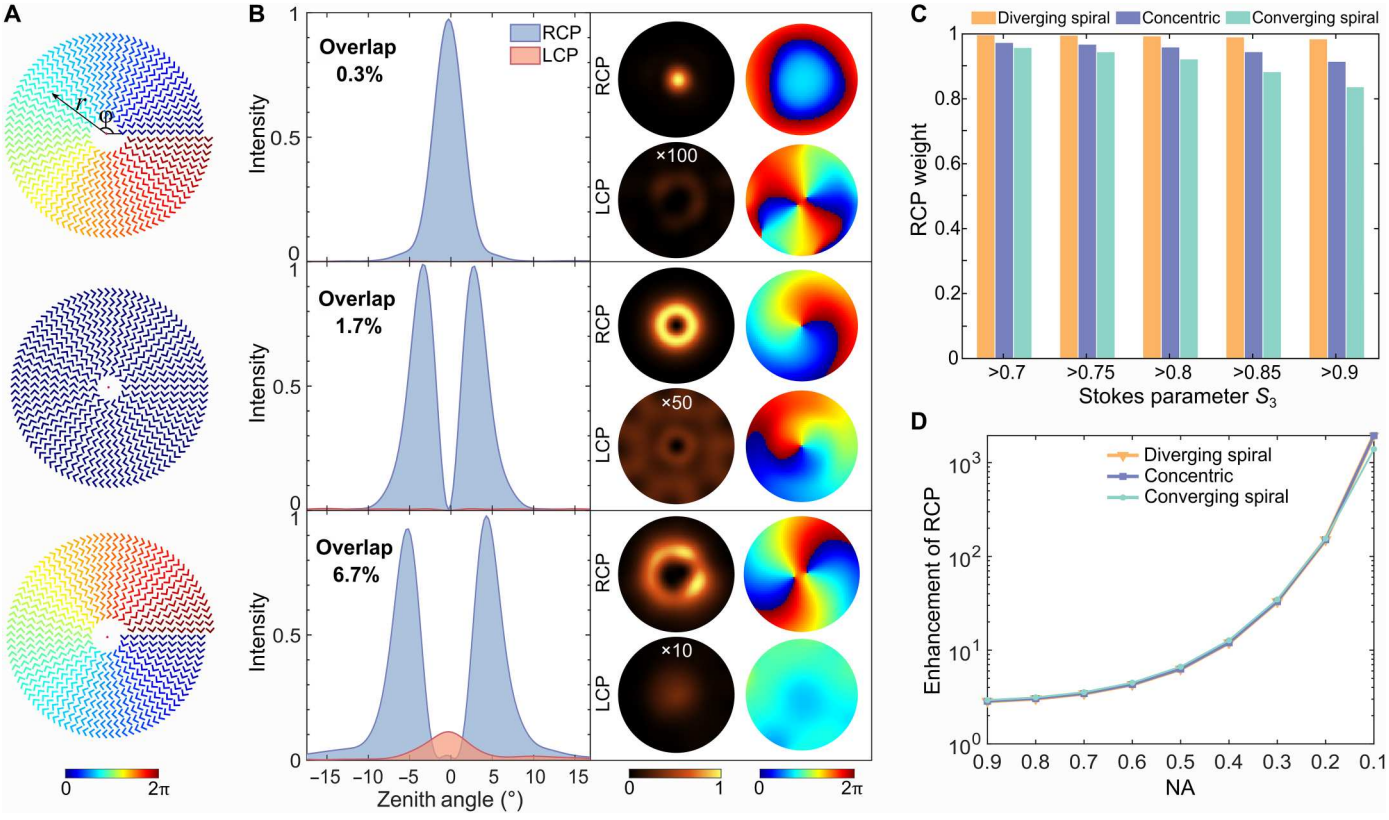

Fig. 2. Generation of single-mode dominated circularly polarized vortex beams. (**A**) DONR azimuthal arrangements for generating high-purity circularly polarized vortices with (from top to bottom) diverging spiral, concentric, and converging spiral trajectories, which are colored according to the SPP propagation phase. (**B**) Simulated intensity and phase distributions of the RCP and LCP contributions for the corresponding configurations. First column: The RCP and LCP intensity profiles with their spatial overlap quantified as 0.3, 1.7, and 6.7%, respectively. Second and third columns: The intensity [numerical aperture (NA) = 0.2] and corresponding phase distributions. The LCP intensity distributions have been enhanced by 100, 50, and 10 times, respectively, to improve their visibility. (**C**) RCP weight indicating the relative RCP contribution in the total emission for the considered configurations and different chirality thresholds. (**D**) Enhancement of the RCP emission with respect to the emission without metasurfaces as a function of the collecting objective NA.

considered to have the same strength with the phases being set in accordance with the SPP propagation phase. The simulation results demonstrated indeed the generation of perfect RCP (LCP contribution of <1%) vortex beams with the corresponding topological charges: ℓ = 0, 1, and 2 (fig. S3). Similar results have been obtained with the mirrored DONR configuration producing perfect LCP vortices. We should note that the analytical derivation of SAM and OAM components generated by arrays of angular-distributed dipoles is, in principle, possible (*45*) but goes beyond the scope of our work limited to the simple model described above. This simple model, which does not require heavy calculations, might also be found useful when analyzing the performance of other QE-coupled metasurfaces. Similar to the orthogonal electric dipoles, the designed DONR with sufficient number of rings can efficiently outcouple SPPs into well-collimated far-field photon emission (figs. S4 to S7). The simulated decay rate enhancement (Purcell factor) with respect to that in free space is ~3.3 with the quantum efficiency (QE), η_{QE}, (the ratio between the radiative and total decay rates) being ~0.32, which is a moderate value due to the use of low-index (n = 1.41) HSQ polymer to fabricate metasurface nanostructures. Outcoupling metasurfaces made of high-index dielectrics would increase the outcoupling efficiency and thereby decrease the influence of SPP absorption, increasing consequently the quantum efficiency (*38*). Thus, in our case, the quantum efficiency can be increased to ~0.73 simply by using TiO_2 (n = 2.56) metasurface nanostructures (fig. S8). Last, because of very good collimation of the outcoupled radiation by the designed metasurfaces, the collection efficiency, η_{CE}, is evaluated to be ~0.9 for the collecting emission objective with the NA = 0.9 (fig. S8).

Demonstration of high-purity SAM states

Following the design described above, various SAM-OAM photon sources were fabricated using NDs containing multiple NVs or single NV centers, respectively (fig. S9). The scanning electron microscopy images of the fabricated metasurfaces with DONRs lined up along different spiral trajectories evidence accurate positioning of NDs with multiple NVs (Fig. 3A) as well as high quality and homogeneity of the fabricated nanostructures (figs. S10 and fig. S11). The performance of photon sources was characterized by evaluating the Stokes parameters (S_0, S_1, S_2, and S_3), in which S_0 represents the total emission intensity; S_1 represents the intensity difference between two orthogonal linear polarizations; S_2 represents the intensity difference between other orthogonal linear polarizations, which are rotated by 45° with respect to the former one; and S_3

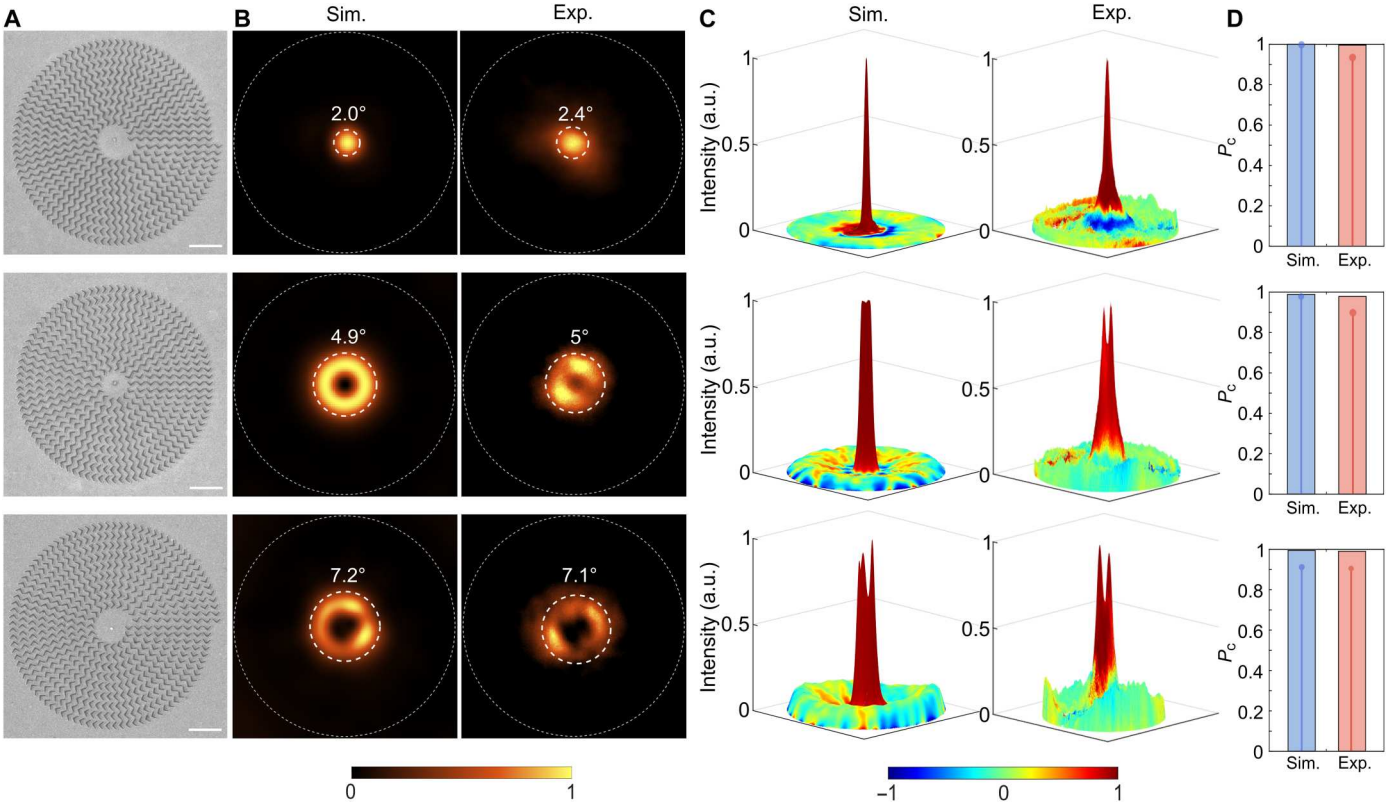

Fig. 3. Demonstration of high-purity SAM states. (**A**) SEM images of the fabricated quantum metasurfaces for generating circularly polarized vortex photon beams. Scale bars, 2 μm for all SEM images. (**B**) Simulated (Sim.) and experimentally (Exp.) measured intensity distributions of the photon emission from the corresponding quantum metasurfaces (NA = 0.3). The white dashed circles encircle the areas corresponding to the full width at half maximum intensities. (**C**) 3D representation of the superimposed intensity and polarization distributions. The height indicates the intensity, and the color indicates the degree of the circular polarization, with the red (blue) color representing the RCP (LCP). (**D**) Intensity-weighted $\overline{P_c}$ and maximum P_c in the high-intensity areas.

represents the intensity difference between the right- or left-hand circular polarizations (all normalized to the total intensity obtained in each measurement) (*37*, *46*, *47*). The Stokes parameters were directly measured with the photon emission passing through a quarter–wave plate and linear polarizer (fig. S12 and note S3). We evaluate the chirality (i.e., the degree of circular polarization) of the observed photon emission using the chiral parameter S_3 weighted with the other parameters: $P_c = S_3/\sqrt{(S_1)^2 + (S_2)^2 + (S_3)^2}$. Far-field photon emission patterns feature well-collimated beams, with a very good correspondence between the simulated and experimentally observed intensity distribution (Fig. 3B and fig. S13). Note that the experimentally obtained divergence angles, 2.4°, 5°, and 7.1°, are very close to those expected from the simulations. The simulated and measured photon emission intensity and polarization distributions superimposed in three-dimensional (3D) representations exhibit a very good correspondence (Fig. 3C), ascertaining the generation of single-mode SAM-OAM beams. To quantitatively characterize the performance with respect to the chirality of generated photon beams, we define the degree of circular polarization averaged over the intensity distribution: $\overline{P_c} = \sum_i P_c(i)I(i)/\sum_i I(i)$. The photon beam chirality can thus be evaluated as the average chirality $\overline{P_c}$ calculated from the high-intensity data area (i.e., within the divergence angle indicated by the dashed line in Fig. 3B). This procedure results in the average beam chirality values of 0.934, 0.902, and 0.893 for the three realized (diverging spiral, concentric, and converging spiral) configurations, respectively. Moreover, the maximum chirality values are measured to be 0.996, 0.978, and 0.991 for these configurations, confirming further the generation of high-purity RCP beams (Fig. 3D).

The OAM states of generated SAM-OAM photon beams were characterized by using a spatial light modulator (SLM), whose reflection was encoded with different orders of spiral phases, to demodulate phase profiles of OAM beams (*39*, *44*). When changing the topological charge of the SLM phase distribution, the azimuthal intensity pattern of a photon beam reflected by the SLM should change in accordance with the topological charge of the generated vortex beam. A bright spot is expected to be formed when the topological charge of the SLM phase is opposite to that of the vortex beam (fig. S14). Our experimental characterization (Materials and Methods) demonstrated that the azimuthal intensity patterns observed for different SLM spiral phase distributions exhibit indeed well-pronounced and concentrated bright spots for the corresponding topological charges of the SLM phase distribution (fig. S15), indicating thereby high quality of the fabricated SAM-OAM photon sources. We have also observed that the metasurfaces composed of the mirrored DONRs result in the generation of high-quality LCP photon Gaussian and vortex beams (fig. S16).

Single-photon single-mode SAM-OAM beams

Following the design, fabrication, and characterization procedures described above (but using NDs containing only single NV centers; fig. S17), we realized and characterized single-photon sources of well-collimated single-mode SAM-OAM beams. The main differences in the results of optical characterization are related to considerably weaker photon signals from the single-photon sources, resulting in the optical images being more influenced by the background noise. Thus, the azimuthal intensity distributions observed for different SLM spiral phase distributions when characterizing three different single-photon sources exhibited essentially the same patterns (Fig. 4A), ascertaining also in this case, with the diverging, concentric, and converging spiral DONR trajectories, the generation of the RCP vortex beams carrying the corresponding topological charges ℓ = 0, +1, and +2. The generated SAM-OAM photon modes were of high purity, especially the Gaussian RCP mode exhibited the impressive mode purity of 81%, with 94% being expected from simulations (Fig. 4, B and C). The second-order correlation functions of photon emission measured before and after NV-ND coupling to the corresponding metasurface feature the zero-delay level $g^{(2)}(0)$ = 0.129 and 0.141, respectively (Fig. 4D), indicating excellent and stable single-photon properties. In addition, the NV-ND lifetimes (fig. S18) and fluorescence spectra of photon emission (Fig. 4C) did not change notably when measured before and after NV-ND coupling to the metasurface. The single-photon emission spectrum obtained after the NV-ND coupling features two zero-phonon lines, appearing at 575 and 637 nm and indicating, respectively, the charge state of NV dominated by negative (NV^-) and neutral (NV^0) charge state (*47*), and the emission peak at ~670 nm, which is the target wavelength of the designed metasurfaces. We note that the proposed design approach is general and can be used for other QEs with different wavelengths and emission decay rates. Regarding the single-photon purity and photon indistinguishability, it has been demonstrated that these two characteristics can be maintained at a very high level (at cryogenic temperatures) even after QE coupling to nanostructures (*48*–*50*).

DISCUSSION

In this work, we proposed the general approach for designing single-photon circularly polarized single-mode vortex beams, with the SAM and OAM states being separately controlled by the DONR configuration and array arrangement. The developed approach provides thereby a straightforward flexible way to precisely engineer the SAM-OAM states of single photons emitted by the DONR-based quantum metasurface. A set of room-temperature single-photon sources has been designed, fabricated, and characterized, demonstrating the generation of high-purity circularly polarized vortex beams by the fabricated QE-coupled quantum metasurfaces. Our successful experimental realizations of high-quality SAM-OAM encoded single-photon sources confirm the robustness of the developed approach with respect to small QE displacements with respect to the DONR arrangement as indicated by the numerical simulations (figs. S6 and S7). This approach can straightforwardly be extended to produce linearly polarized photon beams by interleaving two metasurfaces (*51*), i.e., DONR arrangements for providing the RCP and LCP photons. Interleaving two metasurfaces for generating different SAM-OAM states opens a

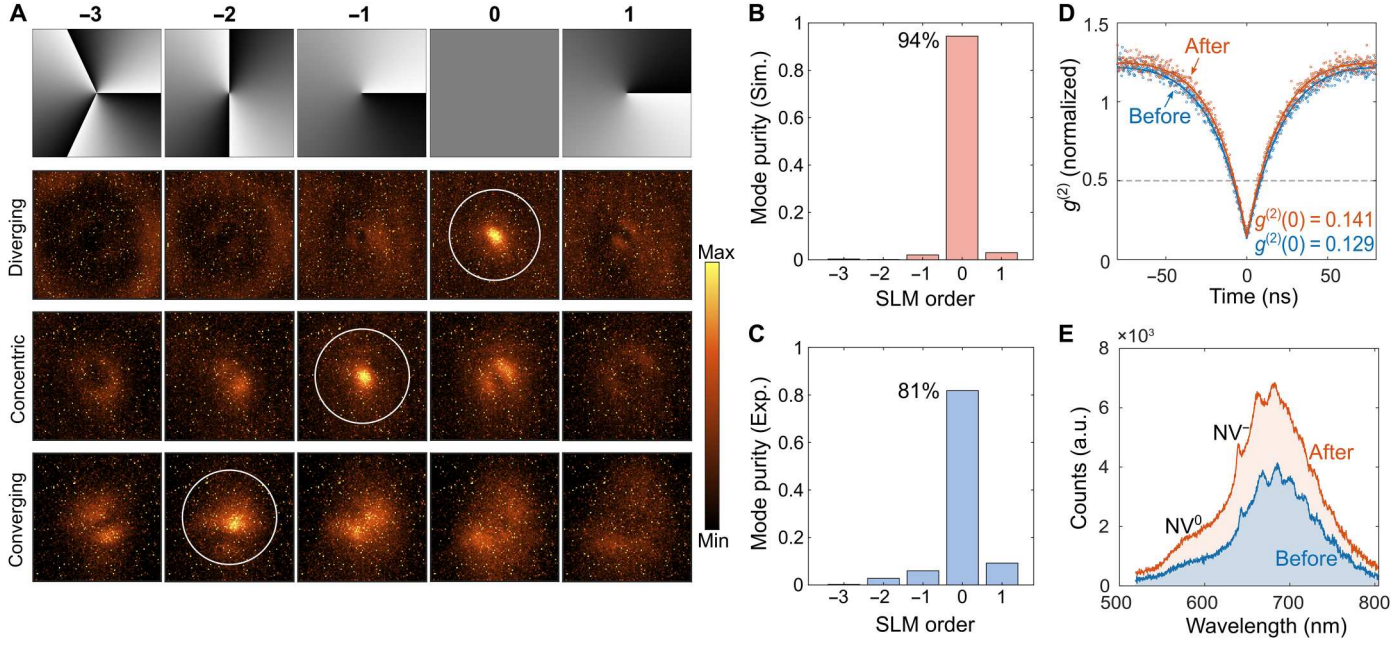

Fig. 4. Characterization of single-photon single-mode SAM-OAM beams. (**A**) Intensity distributions of the single-photon emission obtained with different DONR spiral trajectories measured after the reflection from the SLM encoded with different orders of spiral phases. First row present the phase distribution for the SLM holograms with the topological charges of −3, −2, −1, 0, and 1. Second, third, and fourth rows present the intensity distributions obtained with the diverging, concentric, and converging spiral arrangements, respectively. (**B** and **C**) Mode purity of the single-photon source simulated (B) and measured (C) with the diverging spiral trajectory. (**D**) Second-order correlation function $g^{(2)}$ of single-photon emission measured before and after the ND-NV coupling with the metasurface using 100 μW of 532-nm continuous laser. (**E**) Fluorescence spectrum of the single-photon emission measured before and after the ND-NV coupling.

way for producing entangled SAM-OAM states, similarly to what has recently been demonstrated (*39*), but with a very substantial difference: The total angular momentum of entangled states does not have to be the same—it can be arbitrarily different in accordance with the design of the individual metasurfaces (fig. S19). Moreover, high-order OAM modes can also be realized with the proposed DONR-based quantum metasurfaces by increasing the number of spiral arms (fig. S20). Furthermore, by gradually changing the chirality of composing DONRs, the SAM and OAM of the photon emission can be flexibly manipulated with different ratios (fig. S21). Last, by combining the interleaving procedure (*51*) and recently established holographic formalism (*35*), the general approach developed in this work can further be extended to produce multiple, differently polarized radiation channels and enable thereby realization of high-dimensional quantum sources for advanced quantum photonic technologies. The on-chip room-temperature versatile handling of photon states opens thereby exciting perspectives for designing advanced single-photon sources and would contribute to further developments within chiral quantum optics, concerned with advanced functionalities such as spin/angular controlled photon switching and high-dimensional quantum information processing.

MATERIALS AND METHODS

Numerical simulations

Numerical simulations of QE-coupled metasurfaces were performed with 3D finite-difference time-domain (FDTD) method. A *z*-direction electric dipole was placed 30 nm atop the SiO_2 spacer (with the thickness of 20 nm) and silver film (with thickness of 150 nm) and in the center of dielectric nanostructures (with height of 150 nm and refractive index of 1.41). The wavelength of the dipole was set as 670 nm, fitting the emission peak wavelength of ND-NVs. The period of the metasurfaces was set to be equal to the SPP wavelength (λ_{spp} = 580 nm with the effective SPP mode index n_{spp} = 1.16). The start radius r_0 is $1.7\lambda_{spp}$. The number of windings was $N = 9$, enabling efficiently outcoupling SPPs into well-collimated far-field photon emission (figs. S4 and S5). A 2D monitor 30 nm atop the configuration was used to collect far-filed electric field by near- to far-field transformation method.

Device fabrication

Fabrication of QE-coupled metasurfaces followed a well-established sequence of technological steps (fig. S9) (*37*, *46*). A 150-nm-thick silver film was first deposited on the silicon substrate by the thermal evaporation, followed by a 20-nm-thick SiO_2 layer being deposited by the magnetron sputtering method. Then, a group of gold markers were fabricated on the substrate by the electron beam lithography (EBL), gold deposition, and the lift-off. Subsequently, ND-NVs were spin-coated with proper concentration. After that, the dark-field microscope image or the fluorescence scan image was taken to determine the position of, respectively, multiple or single ND-NVs with the help of alignment markers. It should be noted that the accurate positioning of DONR arrangements with respect to singles NV centers was more problematic as compared to the positioning of NDs with multiple NVs because it had to be relied on fluorescence images (fig. S17) that were noisier than the dark-field images (fig. S9). After determining the position of ND-NVs with the precise alignment procedure, a negative photoresist (HSQ) was subsequently spin-coated at 4000 rpm, for 45 s, and heated at the hotplate on 160°C for 2 min to form a ~150-nm layer, which was examined by the atomic force microscopy (NT-MDT NTEGRA). The EBL direct writing of metasurface patterns was then carried out on the resist around NV-NDs (JEOL-6490 system; accelerating voltage of 30 kV). Last, QE-coupled metasurfaces were obtained by development with the tetramethylammonium hydroxide solution (for 4 min) and isopropanol (60 s).

Optical characterization

Characterization of QE-coupled metasurfaces was conducted using essentially the same experimental setup as in the previous experiments (fig. S12) (*37*, *39*).

Excitation of single photons

A linearly polarized 532-nm continuous wave or pulsed laser beam, after passing through a radially polarized converter (AR Coptix RPC), was used to driven NV-NDs to form a dominant dipole moment perpendicular to the substrate surface. The excitation and collection of emission were by the same objective with NA = 0.9 (×100; The Olympus MPLFLN).

SAM and OAM states measurement

In SAM states, the Stokes parameters (S_0, S_1, S_2, and S_3) were measured to characterize the SAM states. S_1 and S_2 were measured by orienting the linear polarizer and taking Fourier plane images. S_3 was measured by the combination of a quarter-wave plate and a linear polarizer. In OAM states, an SLM working at 670 nm was used to generate the computed holograms with different topological charges. As the SLM only responds to the linear polarized light, the RCP component generated from the QE-coupled metasurface was converted to the linearly polarized photons by a 45°-oriented quarter–wave plate combined with a vertically placed linear polarizer. The reflected light from the incident light was filtered out by a set of dichroic mirrors (Semrock FF535-SDi01/FF552-Di02) and with long-pass filter of 550 nm (Thorlabs FELH0550) and band-pass filter of 676 nm (with 29-nm bandwidth; Edmund Optics).

Single-photon characterization

The photon emission was guided to spectrometer or single-photon detectors for the measurement of correlation, spectrum, and fluorescence image via the flip mirror. Fluorescence imaging (for ND-NV positioning process) was performed by a synchronous movement of piezo stage with mounted sample and projecting the collected fluorescence emission to the avalanche photo diodes (APDs). The decay rate measurements were carried out with a pulsed laser (PicoQuant LDH-PFA-530L) at 1 MHz together with APD1 (τ-SPAD, PicoQuant). Fluorescence spectra were measured using the spectrometer (Andor Ultra 888 USB3-BV) operating within 540 to 820 nm. Second-order correlation was recorded by registering the temporal delay between APD1 and APD2 in a start-stop configuration using an electronic timing box (PicoHarp 300, PicoQuant).

Supplementary Materials

This PDF file includes:

Supplementary Text
Figs. S1 to S21
References

REFERENCES AND NOTES

1. A. Mair, A. Vaziri, G. Weihs, A. Zeilinger, Entanglement of the orbital angular momentum states of photons. *Nature* **412**, 313–316 (2001).
2. G. Molina-Terriza, J. P. Torres, L. Torner, Twisted photons. *Nat. Phys.* **3**, 305–310 (2007).
3. C. H. Bennett, D. P. DiVincenzo, Quantum information and computation. *Nature* **404**, 247–255 (2000).
4. N. Gisin, R. Thew, Quantum communication. *Nat. Photon.* **1**, 165–171 (2007).
5. X.-L. Wang, X.-D. Cai, Z.-E. Su, M.-C. Chen, D. Wu, L. Li, N.-L. Liu, C.-Y. Lu, J.-W. Pan, Quantum teleportation of multiple degrees of freedom of a single photon. *Nature* **518**, 516–519 (2015).
6. A. Sit, F. Bouchard, R. Fickler, J. Gagnon-Bischoff, H. Larocque, K. Heshami, D. Elser, C. Peuntinger, K. Günthner, B. Heim, C. Marquardt, G. Leuchs, R. W. Boyd, E. Karimi, High-dimensional intracity quantum cryptography with structured photons. *Optica* **4**, 1006–1010 (2017).
7. A. Fleischer, O. Kfir, T. Diskin, P. Sidorenko, O. Cohen, Spin angular momentum and tunable polarization in high-harmonic generation. *Nat. Photonics* **8**, 543–549 (2014).
8. P. Lodahl, S. Mahmoodian, S. Stobbe, A. Rauschenbeutel, P. Schneeweiss, J. Volz, H. Pichler, P. Zoller, Chiral quantum optics. *Nature* **541**, 473–480 (2017).
9. A. Javadi, D. Ding, M. H. Appel, S. Mahmoodian, M. C. Löbl, I. Söllner, R. Schott, C. Papon, T. Pregnolato, S. Stobbe, L. Midolo, T. Schröder, A. D. Wieck, A. Ludwig, R. J. Warburton, P. Lodahl, Spin–photon interface and spin-controlled photon switching in a nanobeam waveguide. *Nat. Nanotechnol.* **13**, 398–403 (2018).
10. J. Wang, J.-Y. Yang, I. M. Fazal, N. Ahmed, Y. Yan, H. Huang, Y. Ren, Y. Yue, S. Dolinar, M. Tur, A. E. Willner, Terabit free-space data transmission employing orbital angular momentum multiplexing. *Nat. Photon.* **6**, 488–496 (2012).
11. N. Bozinovic, Y. Yue, Y. Ren, M. Tur, P. Kristensen, H. Huang, A. E. Willner, S. Ramachandran, Terabit-scale orbital angular momentum mode division multiplexing in fibers. *Science* **340**, 1545–1548 (2013).
12. Z.-Y. Zhou, Y. Li, D.-S. Ding, W. Zhang, S. Shi, B.-S. Shi, G.-C. Guo, Orbital angular momentum photonic quantum interface. *Light Sci. Appl* **5**, e16019 (2016).
13. H. H. Arnaut, G. A. Barbosa, Orbital and intrinsic angular momentum of single photons and entangled pairs of photons generated by parametric down-conversion. *Phys. Rev. Lett.* **85**, 286–289 (2000).
14. X. Chen, X. Lu, S. Dubey, Q. Yao, S. Liu, X. Wang, Q. Xiong, L. Zhang, A. Srivastava, Entanglement of single-photons and chiral phonons in atomically thin WSe_2. *Nat. Phys.* **15**, 221–227 (2019).
15. S. Liu, Y. Lou, J. Jing, Orbital angular momentum multiplexed deterministic all-optical quantum teleportation. *Nat. Commun.* **11**, 3875 (2020).
16. G. Li, A. S. Sheremet, R. Ge, T. C. H. Liew, A. V. Kavokin, Design for a nanoscale single-photon spin splitter for modes with orbital angular momentum. *Phys. Rev. Lett.* **121**, 053901 (2018).
17. D. Braukmann, E. R. Glaser, T. A. Kennedy, M. Bayer, J. Debus, Circularly polarized zero-phonon transitions of vacancies in diamond at high magnetic fields. *Phys. Rev. B* **97**, 195448 (2018).
18. I. Söllner, S. Mahmoodian, S. L. Hansen, L. Midolo, A. Javadi, G. Kiršanskė, T. Pregnolato, H. El-Ella, E. H. Lee, J. D. Song, S. Stobbe, P. Lodahl, Deterministic photon–emitter coupling in chiral photonic circuits. *Nat. Nanotechnol.* **10**, 775–778 (2015).
19. B. Chen, Y. Wei, T. Zhao, S. Liu, R. Su, B. Yao, Y. Yu, J. Liu, X. Wang, Bright solid-state sources for single photons with orbital angular momentum. *Nat. Nanotechnol.* **16**, 302–307 (2021).
20. Y. Ma, H. Zhao, N. Liu, Z. Gao, S. S. Mohajerani, L. Xiao, J. Hone, L. Feng, S. Strauf, On-chip spin-orbit locking of quantum emitters in 2D materials for chiral emission. *Optica* **9**, 953–958 (2022).
21. P. G. Kwiat, K. Mattle, H. Weinfurter, A. Zeilinger, A. V. Sergienko, Y. Shih, New high-intensity source of polarization-entangled photon pairs. *Phys. Rev. Lett.* **75**, 4337–4341 (1995).
22. T. Santia-Cruz, S. D. Gennaro, O. Mitrofanov, S. Addamane, J. Reno, I. Brener, M. V. Chekhova, Resonant metasurfaces for generating complex quantum states. *Science* **377**, 991–995 (2022).
23. T. Stav, A. Faerman, E. Maguid, D. Oren, V. Kleiner, E. Hasman, M. Segev, Quantum entanglement of the spin and orbital angular momentum of photons using metamaterials. *Science* **361**, 1101–1104 (2018).
24. K. Wang, J. G. Titchener, S. S. Kruk, L. Xu, H.-P. Chung, M. Parry, I. I. Kravchenko, Y.-H. Chen, A. S. Solntsev, Y. S. Kivshar, D. N. Neshev, A. A. Sukhorukov, Quantum metasurface for multiphoton interference and state reconstruction. *Science* **361**, 1104–1108 (2018).
25. W. J. M. Kort-Kamp, A. K. Azad, D. A. R. Dalvit, Space-time quantum metasurfaces. *Phys. Rev. Lett.* **127**, 043603 (2021).
26. N. Yu, F. Capasso, Flat optics with designer metasurfaces. *Nat. Mater.* **13**, 139–150 (2014).
27. N. Meinzer, W. L. Barnes, I. R. Hooper, Plasmonic meta-atoms and metasurfaces. *Nat. Photon.* **8**, 889–898 (2014).
28. A. V. Kildishev, A. Boltasseva, V. M. Shalaev, Planar photonics with metasurfaces. *Science* **339**, 1232009 (2013).
29. C.-W. Qiu, T. Zhang, G. Hu, Y. Kivshar, Quo Vadis, metasurfaces? *Nano Lett.* **21**, 5461–5474 (2021).
30. Y. Ming, Y. Intaravanne, H. Ahmed, M. Kenney, Y. Lu, X. Chen, Creating composite vortex beams with a single geometric metasurface. *Adv.Mater.* **34**, 2109714 (2022).
31. A. H. Dorrah, F. Capasso, Tunable structured light with flat optics. *Science* **376**, eabi6860 (2022).
32. A. S. Solntsev, G. S. Agarwal, Y. S. Kivshar, Metasurfaces for quantum photonics. *Nat. Photonics* **15**, 327–336 (2021).
33. Y. Kan, F. Ding, C. Zhao, S. I. Bozhevolnyi, Directional off-normal photon streaming from hybrid plasmon-emitter coupled metasurfaces. *ACS Photonics* **7**, 1111–1116 (2020).
34. R. Bekenstein, I. Pikovski, H. Pichler, E. Shahmoon, S. F. Yelin, M. D. Lukin, Quantum metasurfaces with atom arrays. *Nat. Phys.* **16**, 676–681 (2020).
35. Y. Kan, S. I. Bozhevolnyi, Molding photon emission with hybrid plasmon-emitter coupled metasurfaces. *Adv. Optical Mater.* **10**, 2102697 (2022).
36. L. Li, Z. Liu, X. Ren, S. Wang, V. C. Su, M. K. Chen, C. H. Chu, H. Y. Kuo, B. Liu, W. Zang, G. Guo, L. Zhang, Z. Wang, S. Zhu, D. P. Tsai, Metalens-array–based high-dimensional and multiphoton quantum source. *Science* **368**, 1487–1490 (2020).
37. Y. Kan, S. K. H. Andersen, F. Ding, S. Kumar, C. Zhao, S. I. Bozhevolnyi, Metasurface-enabled generation of circularly polarized single photons. *Adv. Mater.* **32**, 1907832 (2020).
38. D. Komisar, S. Kumar, Y. Kan, C. Wu, S. I. Bozhevolnyi, Generation of radially polarized single photons with plasmonic bullseye antennas. *ACS Photonics* **8**, 2190–2196 (2021).
39. C. Wu, S. Kumar, Y. Kan, D. Komisar, Z. Wang, S. I. Bozhevolnyi, F. Ding, Room-temperature on-chip orbital angular momentum single-photon sources. *Sci. Adv.* **8**, eabk3075 (2022).
40. J. Ni, C. Huang, L.-M. Zhou, M. Gu, Q. Song, Y. Kivshar, C.-W. Qiu, Multidimensional phase singularities in nanophotonics. *Science* **374**, eabj0039 (2021).
41. A. Pors, M. G. Nielsen, G. D. Valle, M. Willatzen, O. Albrektsen, S. I. Bozhevolnyi, Plasmonic metamaterial wave retarders in reflection by orthogonally oriented detuned electrical dipoles. *Opt. Lett.* **36**, 1626–1628 (2011).
42. A. Pors, S. I. Bozhevolnyi, Efficient and broadband quarter-wave plates by gap-plasmon resonators. *Opt. Express* **21**, 2942–2952 (2013).
43. S. Kumar, C. Wu, D. Komisar, Y. Kan, L. F. Kulikova, V. A. Davydov, V. N. Agafonov, S. I. Bozhevolnyi, Fluorescence enhancement of a single germanium vacancy center in a nanodiamond by a plasmonic Bragg cavity. *J. Chem. Phys.* **154**, 044303 (2021).
44. A. Forbes, M. De Oliveira, M. R. Dennis, Structured light. *Nat. Photonics* **15**, 253–262 (2021).
45. J. Zhu, Y. Chen, Y. Zhang, X. Cai, S. Yu, Spin and orbital angular momentum and their conversion in cylindrical vector vortices. *Opt. Lett.* **39**, 4435–4438 (2014).
46. H. G. Berry, G. Gabrielse, A. E. Livingston, Measurement of the Stokes parameters of light. *Appl. Optics* **16**, 3200–3205 (1977).
47. S. K. H. Andersen, S. Bogdanov, O. Makarova, Y. Xuan, M. Y. Shalaginov, A. Boltasseva, S. I. Bozhevolnyi, V. M. Shalaev, Hybrid plasmonic bullseye antennas for efficient photon collection. *ACS Photonics* **5**, 692–698 (2018).
48. H. Wang, Y. M. He, T. H. Chung, H. Hu, Y. Yu, S. Chen, X. Ding, M. C. Chen, J. Qin, X. Yang, R. Z. Liu, Z. C. Duan, J. P. Li, S. Gerhardt, K. Winkler, J. Jurkat, L. J. Wang, N. Gregersen, Y. H. Huo, Q. Dai, S. Yu, S. Höfling, C. Y. Lu, J. W. Pan, Towards optimal single-photon sources from polarized microcavities. *Nat. Photonics* **13**, 770–775 (2019).
49. J. Liu, R. Su, Y. Wei, B. Yao, S. F. C. da Silva, Y. Yu, J. Iles-Smith, K. Srinivasan, A. Rastelli, J. Li, X. Wang, A solid-state source of strongly entangled photon pairs with high brightness and indistinguishability. *Nat. Nanotechnol.* **14**, 586–593 (2019).
50. H. Wang, H. Hu, T. H. Chung, J. Qin, X. Yang, J. P. Li, R. Z. Liu, H. S. Zhong, Y. M. He, X. Ding, Y. H. Deng, Q. Dai, Y. H. Huo, S. Höfling, C. Y. Lu, J. W. Pan, On-demand semiconductor source of entangled photons which simultaneously has high fidelity, efficiency, and indistinguishability. *Phys. Rev. Lett.* **122**, 113602 (2019).
51. A. Pors, M. G. Nielsen, S. I. Bozhevolnyi, Plasmonic metagratings for simultaneous determination of Stokes parameters. *Optica* **2**, 716–723 (2015).
52. A. Yariv, P. Yeh, *Optical Waves in Crystals* (Wiley, 1984), vol. 5.

Acknowledgments: We appreciate F. Ding for helpful discussions and Y. Deng for assistance with the experiment. **Funding:** This work was supported by the National Natural Science Foundation of China grant 52120105009 (to C.Z.), National Natural Science Foundation of China grant 62105150 (to Y.K.), European Union's Horizon Europe Research and Innovation Programme under the Marie Skłodowska-Curie Action grant 101064471 (to Y.K.), Natural Science Foundation of Jiangsu Province grant BK20210289 (to Y.K.), Shanghai Key Fundamental Research grant 20JC1414800 (to C.Z.), State Key Laboratory of Advanced Optical Communication Systems Networks of China grant 2022GZKF023 (to Y.K.), and Villum Kann Rasmussen Foundation (award in Technical and Natural Sciences 2019) (to S.I.B.). **Author contributions:** S.I.B. conceived the idea. X.J.L. and Y.H.K. performed theoretical modeling. X.J.L. with assistance from Y.H.K. and D.K. fabricated samples. X.J.L. and Y.H.K. with assistance from

S.K. and D.K. performed experimental measurement. X.J.L., Y.H.K., S. K., and S.I.B. analyzed the data. S.I.B., Y.H.K., and C.Y.Z supervised the project. X.J.L., Y.H.K. and S.I.B wrote the manuscript with contributions from all authors. **Competing interests:** The authors declare that they have no competing interests. **Data and materials availability:** All data needed to evaluate the conclusions in the paper are present in the paper and/or the Supplementary Materials.

Submitted 8 February 2023
Accepted 11 July 2023
Published 9 August 2023
10.1126/sciadv.adh0725

ScienceAdvances

On-chip generation of single-photon circularly polarized single-mode vortex beams

Xujing Liu, Yinhui Kan, Shailesh Kumar, Danylo Komisar, Changying Zhao, and Sergey I. Bozhevolnyi

Sci. Adv., **9** (32), eadh0725.
DOI: 10.1126/sciadv.adh0725

Science Advances
AAAS

Supplementary Materials for

On-chip generation of single-photon circularly polarized single-mode vortex beams

Xujing Liu *et al.*

Corresponding author: Sergey I. Bozhevolnyi, seib@mci.sdu.dk

Sci. Adv. **9**, eadh0725 (2023)
DOI: 10.1126/sciadv.adh0725

This PDF file includes:

Supplementary Text

Note 1: Theoretical analysis of SPP scattering into circularly polarized light

(1) Producing RCP with anisotropic nanobricks

We first introduce conventions for describing the light fields, a plane electromagnetic wave is of the form (*52*):

$$\boldsymbol{E}_{pr}\sim\boldsymbol{E}_0\exp\{i(\omega t-\boldsymbol{k}\cdot\boldsymbol{r})\}\ \rightarrow\boldsymbol{E}_{pr}\sim\boldsymbol{E}_0\exp(-i\boldsymbol{k}\cdot\boldsymbol{r}) \tag{S1}$$

where $\boldsymbol{E}_0$ is the electric field vector, ω is the angular frequency, the wave vector is, $\boldsymbol{k}=2\pi/\lambda$, λ is the wavelength of the wave. For a right-hand circularly polarized (RCP) wave travelling in the +*z* direction:

$$\boldsymbol{E}_{pr}\sim E_0\frac{1}{\sqrt{2}}\begin{pmatrix}1\\-i\end{pmatrix}\exp\{i(\omega t-\boldsymbol{k}\cdot\boldsymbol{r})\}\sim E_0\begin{pmatrix}1\\-i\end{pmatrix}\exp(-ikz) \tag{S2}$$

We consider the SPP incidence on a doublet of (extremely) anisotropic scatterers displaced by a quarter of the SPP wavelength along the propagation direction as shown in fig. S1A, considering only the in-plane (*x*, *y*) field components, the incident SPP field has only one component:

$$\boldsymbol{E}_{SPP}\sim E_0(1,\ 0)\exp(-ik_{SPP}x) \tag{S3}$$

The (largest) field component scattered by this doublet in the *z* direction can be written as follows:

$$\boldsymbol{E}_{scl}\sim C_1\begin{pmatrix}1+\exp\left(-i\frac{\pi}{2}\right)\\-1+\exp\left(-i\frac{\pi}{2}\right)\end{pmatrix}=C_1\begin{pmatrix}1-i\\-1-i\end{pmatrix}=C_1(1-i)\cdot\begin{pmatrix}1\\-i\end{pmatrix}\sim C_1\cdot e^{-i\frac{\pi}{4}}\cdot\begin{pmatrix}1\\-i\end{pmatrix} \tag{S4}$$

If we consider the contributions from the short side of a nanobrick, the scattered field component is relatively small and can then be written as follows:

$$\boldsymbol{E}_{scs}\sim C_2\begin{pmatrix}1+\exp\left(-i\frac{\pi}{2}\right)\\1-\exp\left(-i\frac{\pi}{2}\right)\end{pmatrix}=C_2\begin{pmatrix}1-i\\1+i\end{pmatrix}\sim C_2\cdot e^{-i\frac{\pi}{4}}\cdot\begin{pmatrix}1\\i\end{pmatrix} \tag{S5}$$

Conclusions:

1) The largest scattered field components produce an RCP wave travelling in the +*z* direction (i.e., towards us), while the minor scattered field components result in an LCP wave travelling in the +*z* direction ($C_1\gg C_2$).
2) The net scattering in both cases is coming from the doublet centre as reflected by the factor $e^{-i\frac{\pi}{4}}$.

(2) Producing RCP vortices

Considering the SPP field propagating under an azimuthal angle φ with the *x*-axis (fig. S1B), the largest contribution to the scattered field can be expressed as follows:

$$\boldsymbol{E}_{scl}(\varphi)\sim C_1\cdot\begin{bmatrix}\cos\varphi & -\sin\varphi\\ \sin\varphi & \cos\varphi\end{bmatrix}\cdot\begin{pmatrix}1\\-i\end{pmatrix}=C_1\begin{pmatrix}\cos\varphi+i\sin\varphi\\ \sin\varphi-i\cos\varphi\end{pmatrix}=C_1e^{i\varphi}\begin{pmatrix}1\\-i\end{pmatrix} \tag{S6}$$

Consequently, the minor contribution to the scattered field can be expressed as follows:

$$\boldsymbol{E}_{scs}(\varphi)\sim C_2\cdot\begin{bmatrix}\cos\varphi & -\sin\varphi\\ \sin\varphi & \cos\varphi\end{bmatrix}\cdot\begin{pmatrix}1\\i\end{pmatrix}=C_2\begin{pmatrix}\cos\varphi-i\sin\varphi\\ \sin\varphi+i\cos\varphi\end{pmatrix}=C_2e^{-i\varphi}\begin{pmatrix}1\\i\end{pmatrix} \tag{S7}$$

Conclusions:

1) The largest scattered field components originating from concentric circles of doublets (separated by the SPP wavelength) produce an RCP vortex field with the +1 topological

charge travelling in the $+z$ direction (i.e., towards us), while the minor scattered field components result in an LCP vortex field with the -1 topological charge.

2) Considering the largest scattered field components producing RCP fields, in order to produce an RCP wave (without topological charges) one should have a diverging (from the centre) spiral of nano-bricks with the distance from the centre (QE) increasing with the angle φ:

$$\varphi = k_{SPP} \cdot \delta r(\varphi) \rightarrow r(\varphi) = r_0 + \frac{\varphi}{k_{SPP}} \tag{S8}$$

In order to add the compensating phase:

$$\boldsymbol{E}_{SPP}(\varphi) \sim E_0 \begin{pmatrix} \cos\varphi \\ \sin\varphi \end{pmatrix} \exp(-ik_{SPP}r) \sim \exp(-i\varphi) \tag{S9}$$

3) Using converging (towards the centre) spiral would result in an RCP vortex field with the +2 topological charge travelling in the $+z$ direction.

4) In order to produce an RCP vortex with the -1 topological charge, one should use a twice fast diverging spiral:

$$2\varphi = k_{SPP} \cdot \delta r(\varphi) \rightarrow r(\varphi) = r_0 + \frac{2\varphi}{k_{SPP}} \tag{S10}$$

The compensating phase is:

$$\boldsymbol{E}_{SPP}(\varphi) \sim E_0 \begin{pmatrix} \cos\varphi \\ \sin\varphi \end{pmatrix} \exp(-ik_{SPP}r) \sim \exp(-i2\varphi) \tag{S11}$$

(3) Producing LCP with anisotropic nanobricks

We consider then the SPP incidence on a mirrored doublet of (extremely) anisotropic scatterers displaced by a quarter of the SPP wavelength along the propagation direction as shown in fig. S1C: The (largest) field scattered by this doublet in the z direction can be written as follows:

$$\boldsymbol{E}_{scl} \sim C_1 \left(1 + exp\left(-i\frac{\pi}{2}\right), -1 + exp\left(-i\frac{\pi}{2}\right)\right) = C_1 \begin{pmatrix} 1-i \\ -1-i \end{pmatrix}$$

$$= C_1(1-i) \cdot \begin{pmatrix} 1 \\ \frac{-1-i}{1-i} \end{pmatrix} = C_1(1-i) \cdot \begin{pmatrix} 1 \\ -i \end{pmatrix} \sim C_1 \cdot e^{-i\frac{\pi}{4}} \cdot \begin{pmatrix} 1 \\ -i \end{pmatrix} \tag{S12}$$

If we consider the contributions from the short side of a nanobrick, the scattered field can then be written as follows:

$$\boldsymbol{E}_{scs} \sim C_2 \left(1 + \exp\left(-i\frac{\pi}{2}\right), -1 + \exp\left(-i\frac{\pi}{2}\right)\right) = C_2 \begin{pmatrix} 1-i \\ -1-i \end{pmatrix} \sim C_2 \cdot e^{-i\frac{\pi}{4}} \cdot \begin{pmatrix} 1 \\ -i \end{pmatrix} \tag{S13}$$

(4) Producing LCP vortices

Considering the SPP field propagating under the angle φ with the x-axis as shown in fig. S1D, the largest contribution to the scattered field can be expressed as follows:

$$\boldsymbol{E}_{scl}(\varphi) \sim C_1 \cdot \begin{bmatrix} \cos\varphi & -\sin\varphi \\ \sin\varphi & \cos\varphi \end{bmatrix} \cdot \begin{pmatrix} 1 \\ i \end{pmatrix} = C_1 \begin{pmatrix} \cos\varphi - i\sin\varphi \\ \sin\varphi + i\cos\varphi \end{pmatrix} = C_1 e^{-i\varphi} \begin{pmatrix} 1 \\ i \end{pmatrix} \tag{S14}$$

Consequently, the minor contribution to the scattered field can be expressed as follows:

$$\boldsymbol{E}_{scs}(\varphi) \sim C_2 \cdot \begin{bmatrix} \cos\varphi & -\sin\varphi \\ \sin\varphi & \cos\varphi \end{bmatrix} \cdot \begin{pmatrix} 1 \\ -i \end{pmatrix} = C_2 \begin{pmatrix} \cos\varphi + i\sin\varphi \\ \sin\varphi - i\cos\varphi \end{pmatrix} = C_2 e^{i\varphi} \begin{pmatrix} 1 \\ -i \end{pmatrix} \tag{S15}$$

Conclusions:

1) The largest scattered field components originating from concentric circles of doublets (separated by the SPP wavelength) produce an LCP vortex field with the -1 topological charge travelling in the $+z$ direction, while the minor scattered field components result in an RCP vortex field with the +1 topological charge.

2) Considering the largest scattered field components producing LCP fields, in order to produce an LCP wave (without topological charges) one should have a converging (to the centre) spiral of nano-bricks with the distance from the centre (QE) decreasing with the angle φ:

$$\varphi = -k_{SPP} \cdot \delta r(\varphi) \rightarrow r(\varphi) = r_0 - \frac{\varphi}{k_{SPP}} \quad \text{(S16)}$$

In order to add the compensating phase:

$$\boldsymbol{E}_{SPP}(\varphi) \sim E_0(\cos\varphi, \sin\varphi) \exp(-ik_{SPP}r) \sim \exp(i\varphi) \quad \text{(S17)}$$

3) Using diverging (from the centre) spiral would result in an LCP vortex field with the -2 topological charge travelling in the $+z$ direction (with the strategy for producing positive topological charges being reversed).

(5) Concluding remarks

The ratio between the strongest and weakest scattered field components is determined by the length-to-width ratio of nanorods (nanobricks or anisotropic scatterers) but is not directly proportional to that. The corresponding dependence is influenced by the nanobrick shape and includes the nanobrick height and the refractive index as well. Nanofabrication along with the design principle limits the largest length-to-width ratio that can realistically be fabricated. For example, it is often very difficult to fabricate a nanobrick with the width smaller than the height. Given the nanobrick separation equal to a quarter of the SPP wavelength implies that the nanobrick length is limited to $\sqrt{2}\lambda_{SPP}/4$ to avoid the overlap of two orthogonal nanobricks (fig. S1). Finally, the scattering strength should not be too small for the out-of-plane SPP scattering being stronger than the SPP absorption, and that requires to fabricate nanobricks with sufficiently large volumes, i.e., with sufficiently large heights. It is then clear that the overall optimization would require to use nanobrick materials with larger refractive indexes, relaxing thereby the requirements of large volumes (the scattering strength increases with the refractive index contrast). Our choice of the nanobrick parameters [Fig. 1B in the main text] is a result of numerical optimization involving extensive simulations and backed up with the control experiments.

Note 2. Experiment of SPP scattering into circularly polarized light

With the numerical simulations showing that the surface plasmon polaritons could be efficiently outcoupled to free-space circular polarized light by the designed anisotropic element, here, we conducted experimental characterization to investigate the performance of anisotropic units, which is the elementary component for the SPP coupler (metasurface B shown in Fig. 3(a)). The excitation of propagating SPPs is realized by a grating A (HSQ) on SiO_2 (20 nm) /Ag (150 nm) substrate. The period is 580 nm with the width of 140 nm, enabling the excitation of SPP with 670 nm laser light. The distance between grating A and metasurface B is 10 μm, considering the trade-off between the overlap of incident beam and outcoupling light and the SPP loss along propagation. A wavelength-tuneable continuous-wave laser (NKT, SuperK EXTREME/FIANIUM) is used as the incident light after converting to TM wave with a polarizer, then focused on the centre of the grating A. As clearly shown in Fig. 3(b), SPP can be excited and then coupling out by metasurface B, confirming its ability for acting as an efficient SPP outcoupler. To characterize the polarized states, a quarter wave plate and linear polarizer is inserted before the CMOS camera to measure the Stokes parameter S_3 (shown in the Fig. 3(c)). Fig. 3(d) shows the 2D distribution of S_3. Reflected light of grating A keeps the linear polarization, while the

outcoupling emission from metasurface B is circular polarized with S_3 = 0.98. It proves that the SPPs can be efficiently outcoupled to free-space circular polarized light by the designed anisotropic element.

Note 3. Polarization measurement

The Stokes polarization parameters are directly measurable based on intensity quantities. The emitted light pass through a quarter wave plate (retardation angle φ), then followed by a linear polarizer with its transmission axis aligned at an angle θ to the x axis. The emitted light of the single photon source can be decomposed as:

$$E_x(t) = E_{0x}e^{i\delta_x}.e^{i\omega t} = E_x e^{i\omega t} \quad \text{(S18)}$$

$$E_y(t) = E_{0y}e^{i\delta_y}.e^{i\omega t}E_y e^{i\omega t} \quad \text{(S19)}$$

where E_x and E_y are the complex amplitude. The Stokes parameter for a plane wave can be obtained from:

$$\begin{aligned} S_0 &= E_x E_x^* + E_y E_y^* \\ S_1 &= E_x E_x^* - E_y E_y^* \\ S_2 &= E_x E_y^* + E_y E_x^* \\ S_3 &= i(E_x E_x^* + E_y E_y^*) \end{aligned} \quad \text{(S20)}$$

where E_x^* and E_y^* are the complex conjugates of E_x and E_y.

The intensity $I(\varphi, \theta)$ of the emitted light is a function of retardation angle φ and polarizer alignment angle θ:

$$I(\varphi,\theta) = E_x E_x^* \cos^2\theta + E_y E_y^* \sin^2\theta + E_x^* E_y e^{-i\varphi}\sin\theta\cos\theta + E_x E_y^* e^{-i\varphi}\sin\theta\cos\theta \quad \text{(S21)}$$

The intensities at four different pairs of φ and θ are measured to calculate the four Stokes parameter. The first three Stokes parameter is measured by rotating the polarizer to angle $\theta = 0°$, $90°$, $45°$, and $-45°$ respectively (remove the quarter wave plate). The final parameter S_3 is measured by the quarter wave retarder ($\theta = \pm 45°, \varphi = 90°$) and linear polarizer ($\theta = 0°$). The Stokes parameter is derived as:

$$\begin{aligned} S_0 &= I(0°,0°) + I(90°,0°) \\ S_1 &= I(0°,0°) - I(90°,0°) \\ S_2 &= I(45°,0°) - I(-45°,0°) \\ S_3 &= I(45°,90°) - I(-45°,90°) \end{aligned} \quad \text{(S22)}$$

The degree of circular polarization of photon emission is defined as

$$P_c = S_3/\sqrt{(S_1)^2 + (S_2)^2 + (S_3)^2} \quad \text{(S23)}$$

in which S_1, S_2, and S_3 are the Stokes parameters normalized to the corresponding total intensity (S_0) obtained in each measurement.

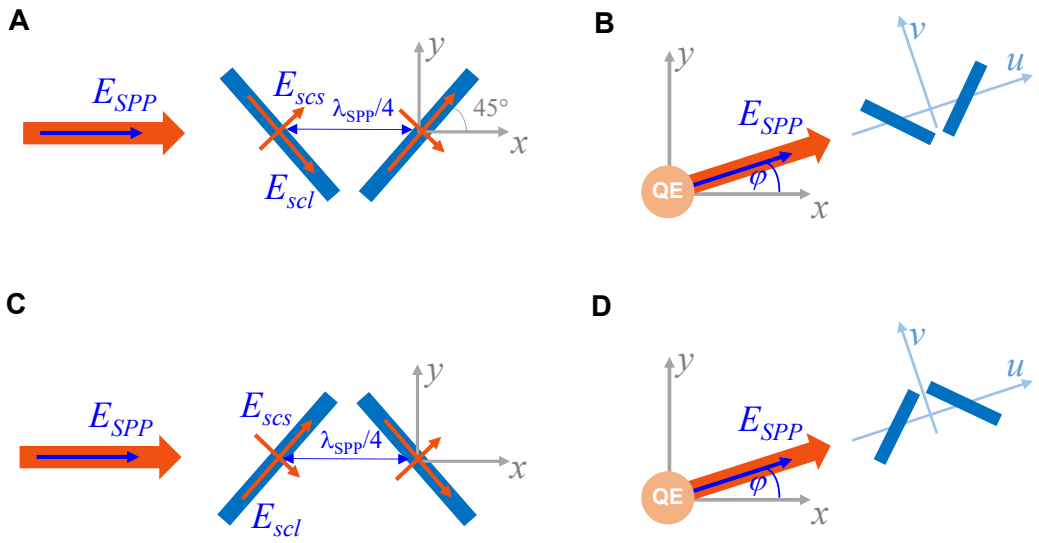

Fig. S1.

Schematic illustration of generating RCP and LCP. (**A, C**) Normal incident SPP scattered by a doublet of anisotropic scatterers. (**B, D)** Regime of QE-excited SPPs propagating under an azimuthal angle φ.

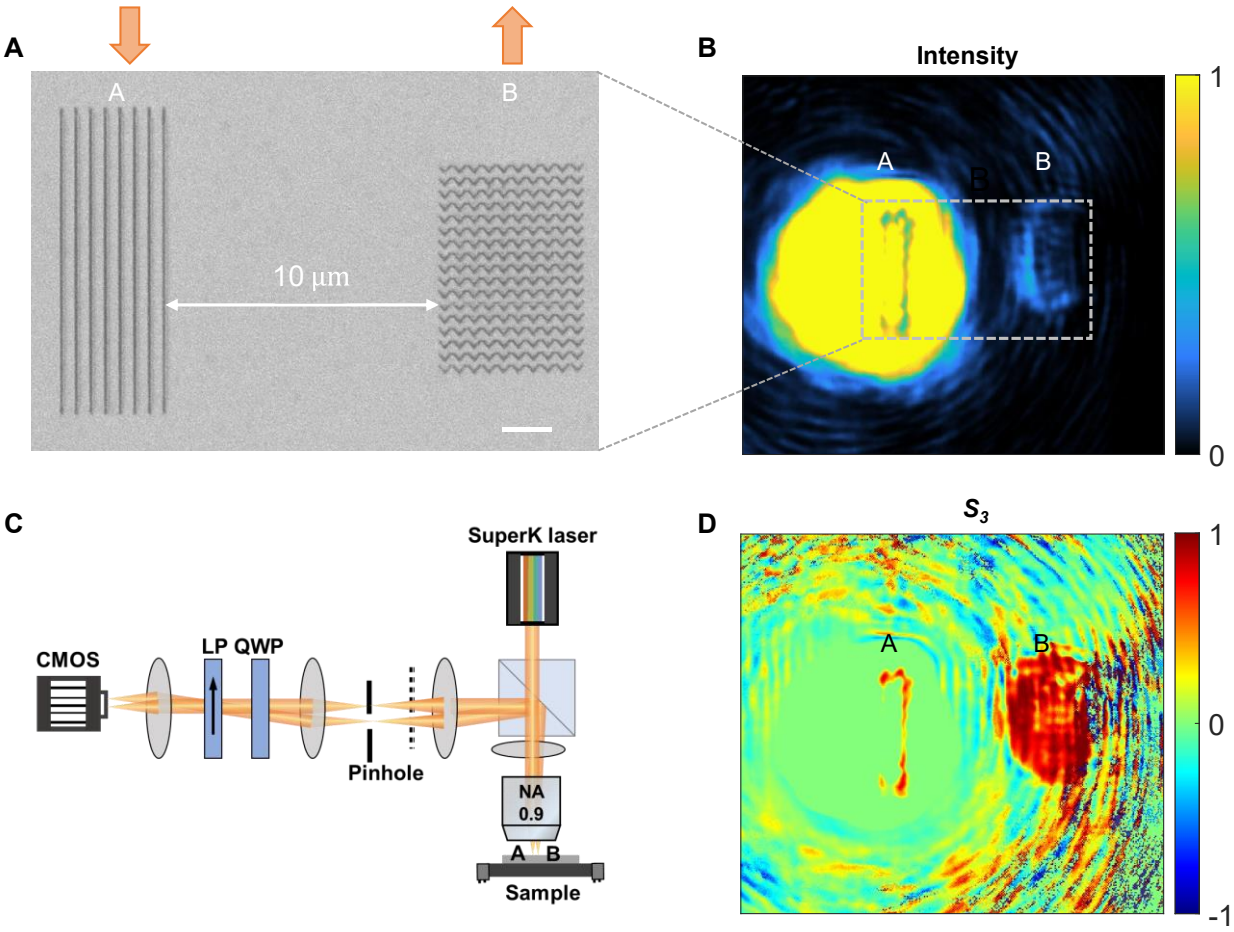

Fig. S2.

Experimental demonstration of RCP generation with optimized element. (**A**) SEM images of the fabricated grating-metasurface. Scale bar: 2 μm. (**B**) The real plane under TM incidence at 670 nm. (**C**) Corresponding experimental setup. (**D**) Measured Stokes parameter S_3.

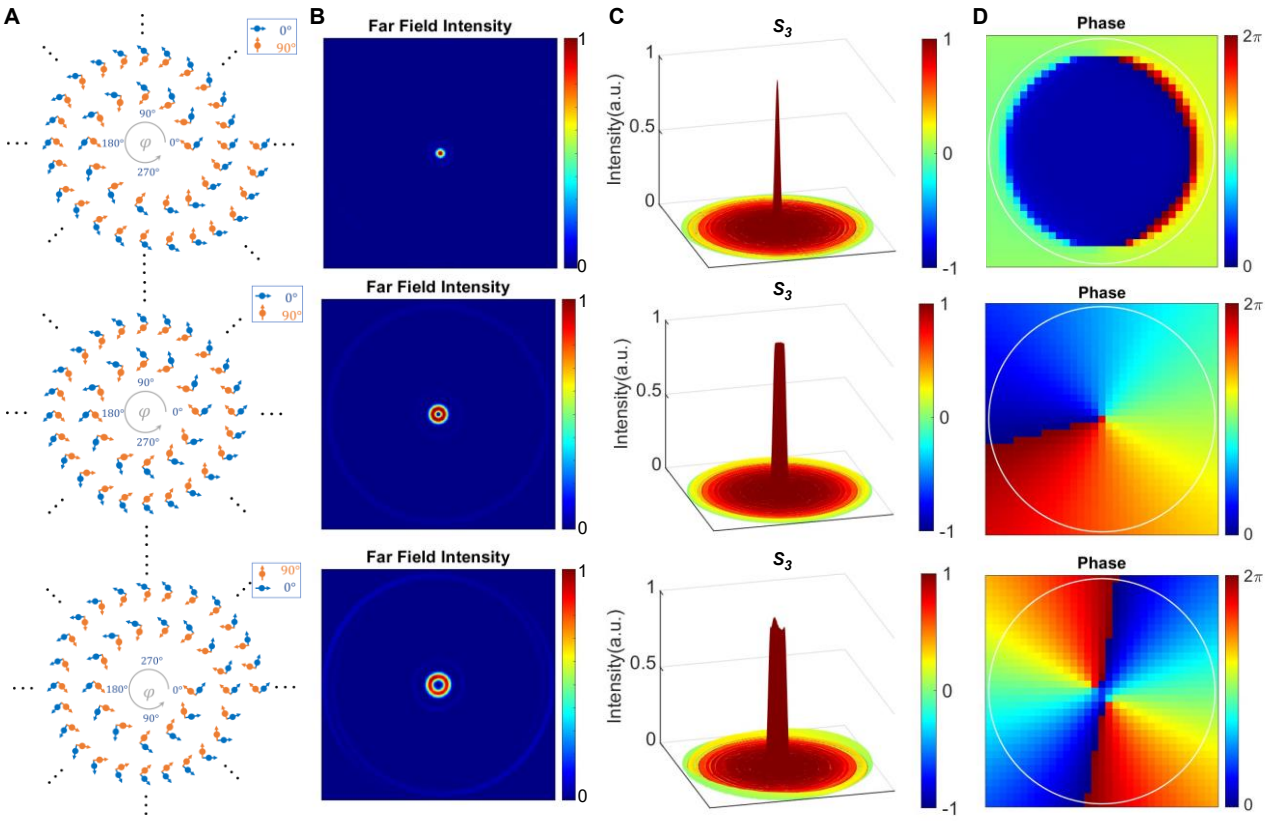

Fig. S3.

Simulated results with dipole arrays, mimicking the designed configuration. (**A**) Schematic of the orthogonal dipole unit arranged with diverging spiral, concentric circle and converging spiral trajectories. There is a phase shift between the orthogonal dipole for each unit, forming perfect circular polarization. (**B**) Far-field angular intensity distribution (in the Fourier plane). (**C**) 3D superimposed intensity and polarization states, the colour shows the Stokes parameter S_3. (**D**) Phase distribution of the decomposed RCP component. The white circle shows the collection angle of NA = 0.1.

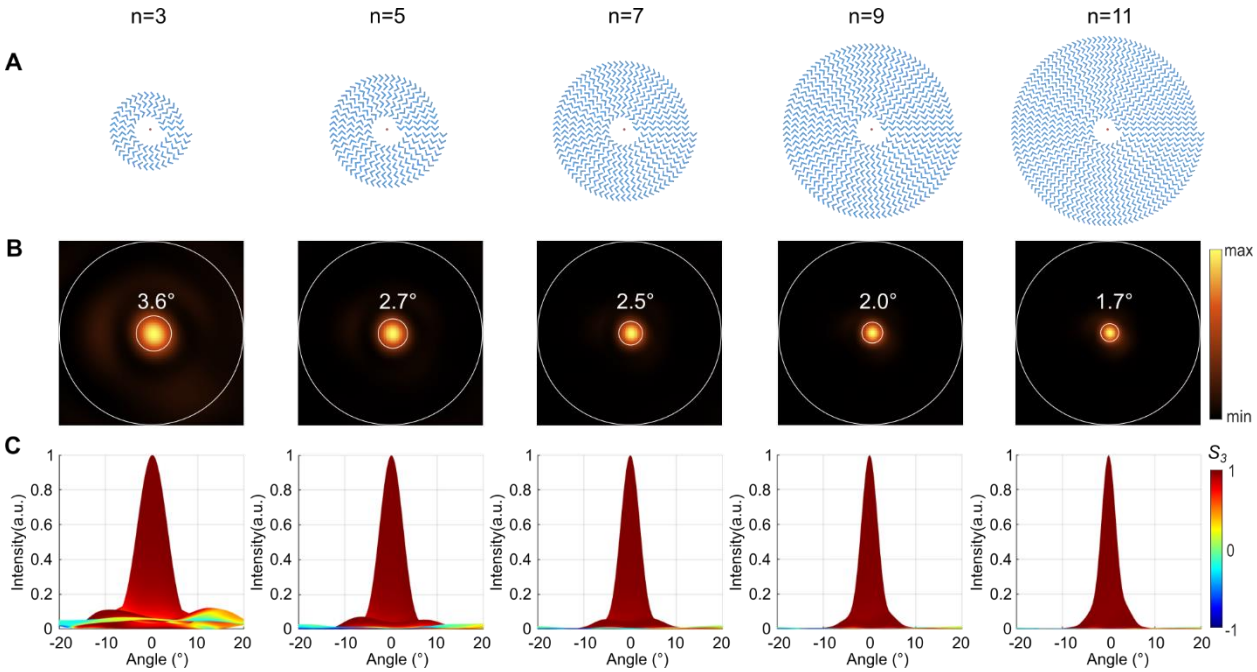

Fig. S4.

Influence of the number of rings on the performance. (**A**) Top view of diverging Archimedean spiral configurations with different number windings (n = 3, 5, 7, 9, and 11). (**B**) Far-field intensity distribution with numerical aperture NA = 0.2. The inner circle denotes the divergence angle. (**C**) The superimposed intensity and degree of circular polarization (the colour represents Stokes parameter S_3).

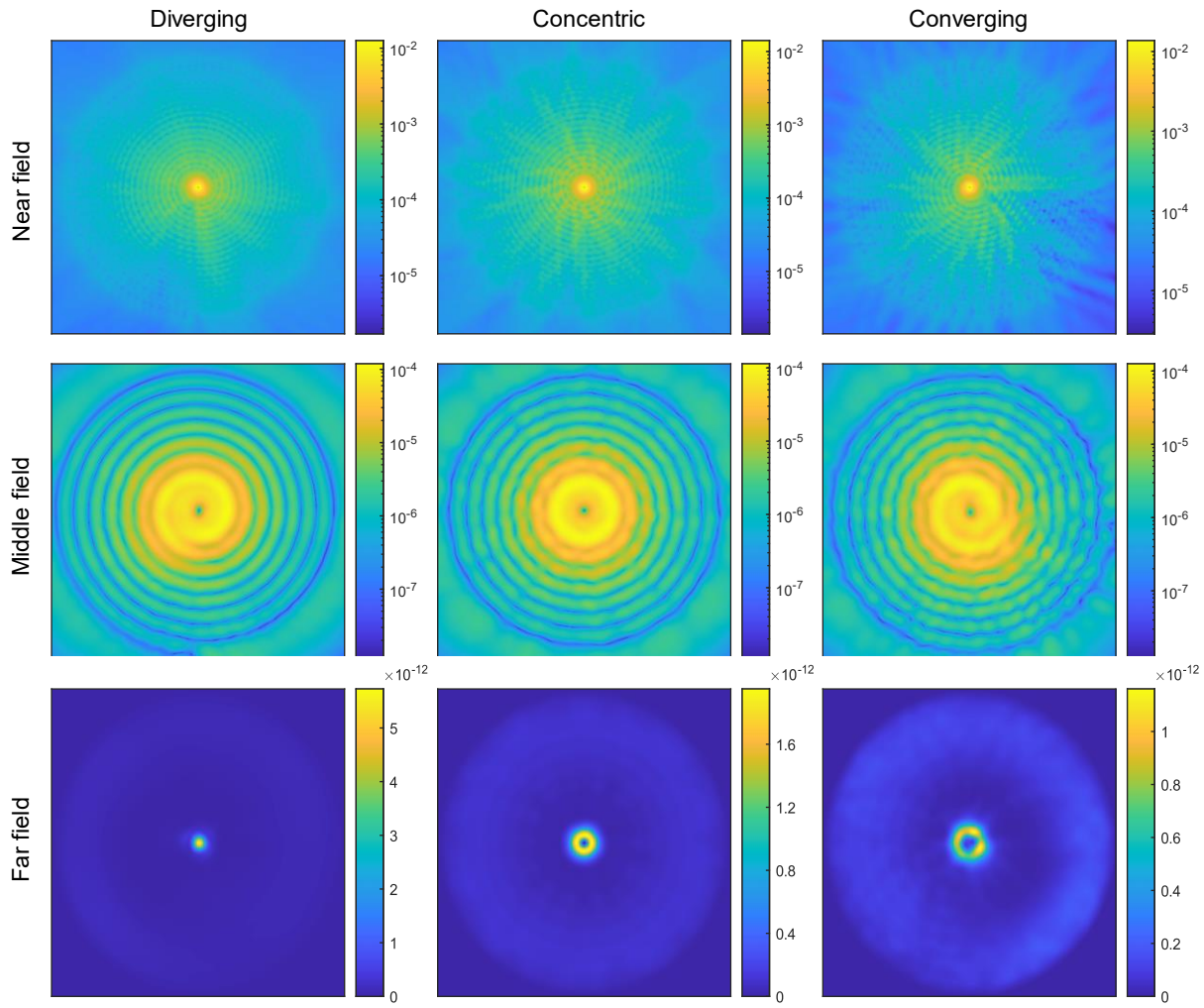

Fig. S5.

Numerical simulations of energy flow (Poynting vector P_z) with designed diverging, concentric, and converging configurations. In the near field, monitor is 30 nm away from metasurface. In the middle field, monitor is 900 nm away from metasurface, the far field is calculated with near to far field transformation. The results present the evolution of energy flow from the dipole source: In the near field, the photon emission is dominated by the dipole source itself; In the middle field, it shows the interactions between the dipole-excited SPPs with the surrounding nanostructures; In the far field, the dipole-excited SPPs are coupled into free space photon emission with different phase profiles (topological charges), showing a bright spot or doughnuts.

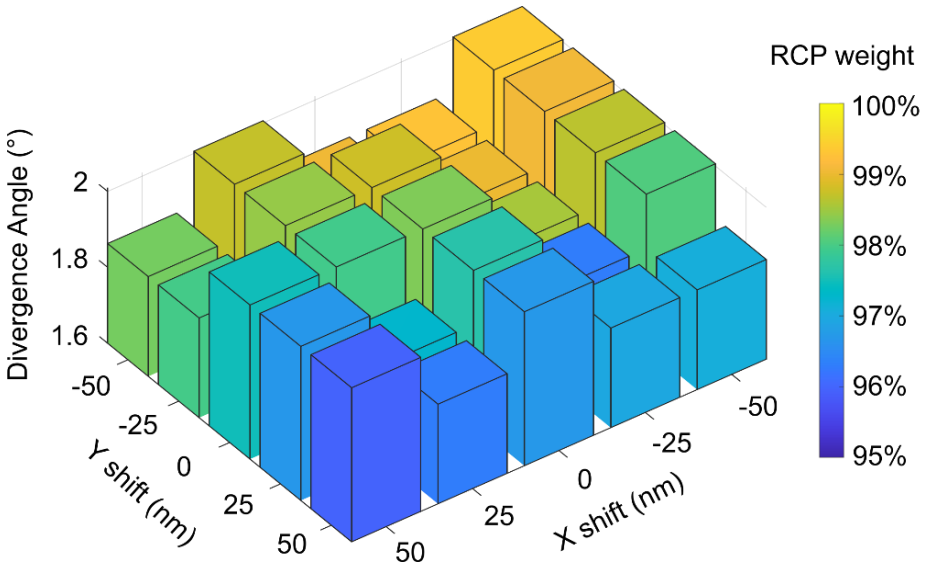

Fig. S6.

Influence of the position shift of QEs on the performance with diverging spiral configuration. The circular polarization purity maintains high value (lager than 95%) and the divergence angle varies from 1.86° to 2°, which are all robust to the position shift of QEs within 50 nm.

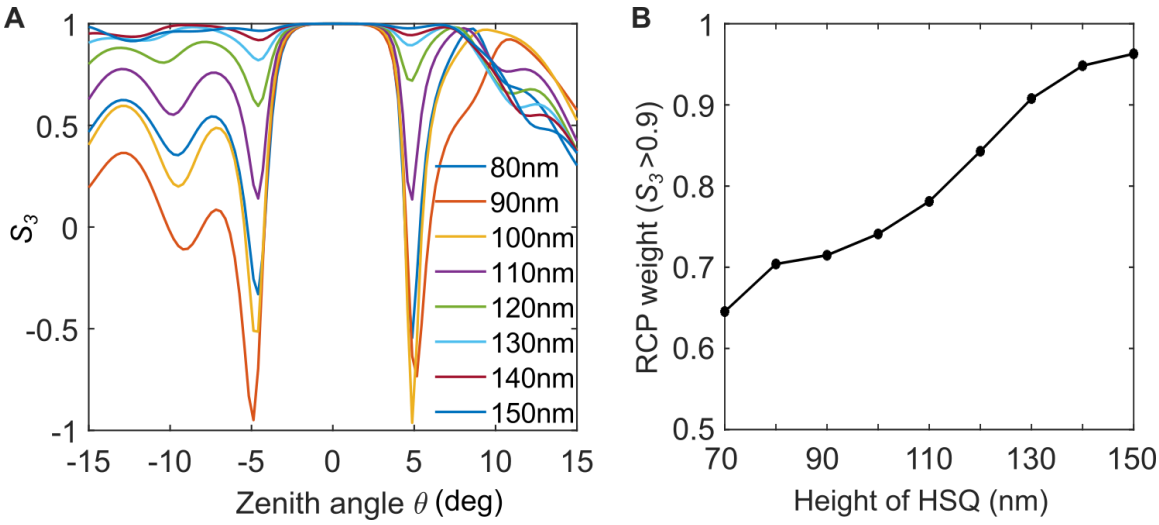

Fig. S7.

Influence of the height of HSQ on the performance of circular polarized states. (**A**) Simulated Stokes parameter S_3 within zenith angle $\pm 15°$. (**B**) Variation of RCP purity with the height of HSQ.

A

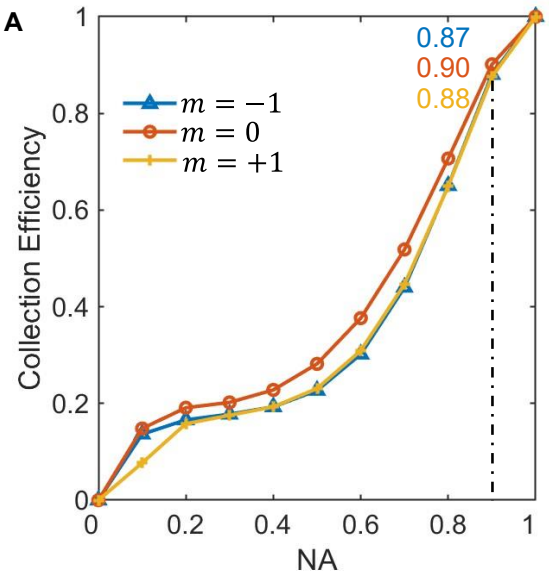

B

Quantum efficiency(TiO_2)	**72.8%**
Quantum efficiency(HSQ)	**32.4%**
Purcell Factor (TiO_2)	**3.53**
Purcell Factor (HSQ)	**3.27**

Fig. S8.

Simulated collection efficiency, quantum efficiency and Purcell factor. (**A**) Collection efficiency as a function of the NA for configurations with diverging spiral ($m = -1$), concentric circle ($m = 0$), and converging spiral ($m = +1$) trajectories. (**B**) Quantum efficiency and Purcell factor with different materials (HSQ and TiO_2) for configuration with diverging spiral ($m = -1$).

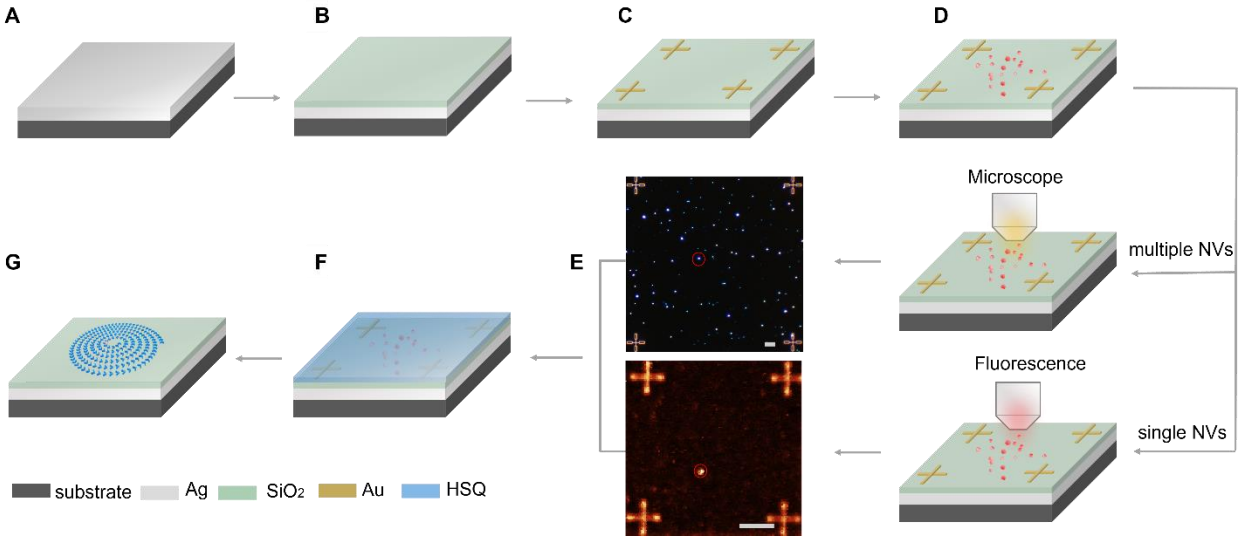

Fig. S9.

Fabrication process of photon sources with multiple ND-NVs and single ND-NV. (**A**) Deposition of 150 nm Ag on the silicon substrate. (**B**) 20 nm SiO_2 deposition. (**C**) The alignment gold markers are fabricated by using EBL, gold deposition, and lift-off process. (**D**) Spin coating nanodiamond containing NVs. (**E**) Determine the position of ND-NVs. A dark-field microscope image is taken to determine the position of ND-NVs. Single-photon ND-NVs is searched by the fluorescence scan with a radially polarized excitation laser beam (532 nm), the position of which is determined by the fluorescence image with the help of alignment markers at the corners of a 27×27 μm^2 area. Scale bar: 5 μm. (**F**) Spin coating HSQ and baked at the hotplate to form 150 nm HSQ layer. (**G**) Metasurfaces are fabricated around the ND-NVs by EBL and the precise alignment procedure. The alignment and position determining method can be found in Ref *(37)*.

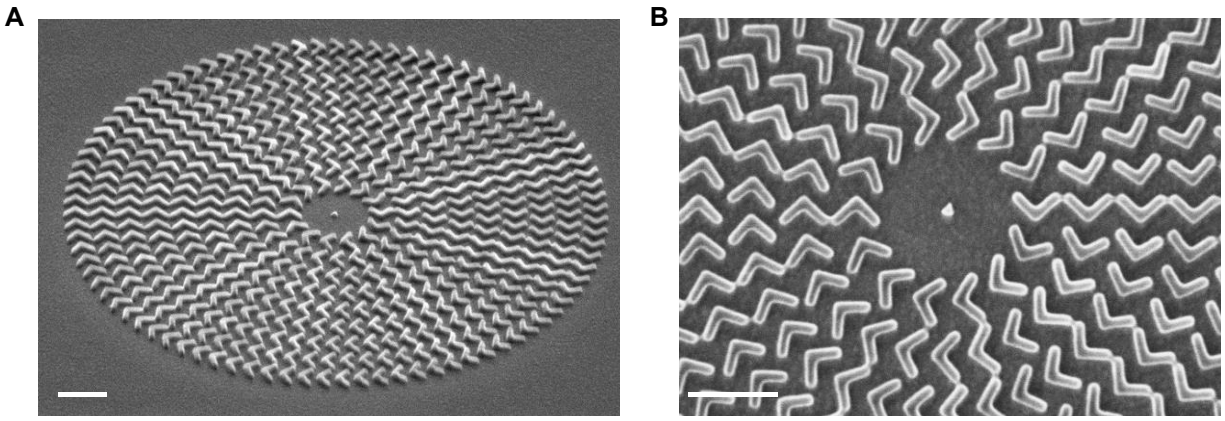

Fig. S10.

SEM of the fabricated devices. (**A**) Angular-view scanning electron micrograph. (**B**) Top-view SEM images of the centre part. ND-NVs is positioned in the center of metasurface. Scale bar: 1 μm.

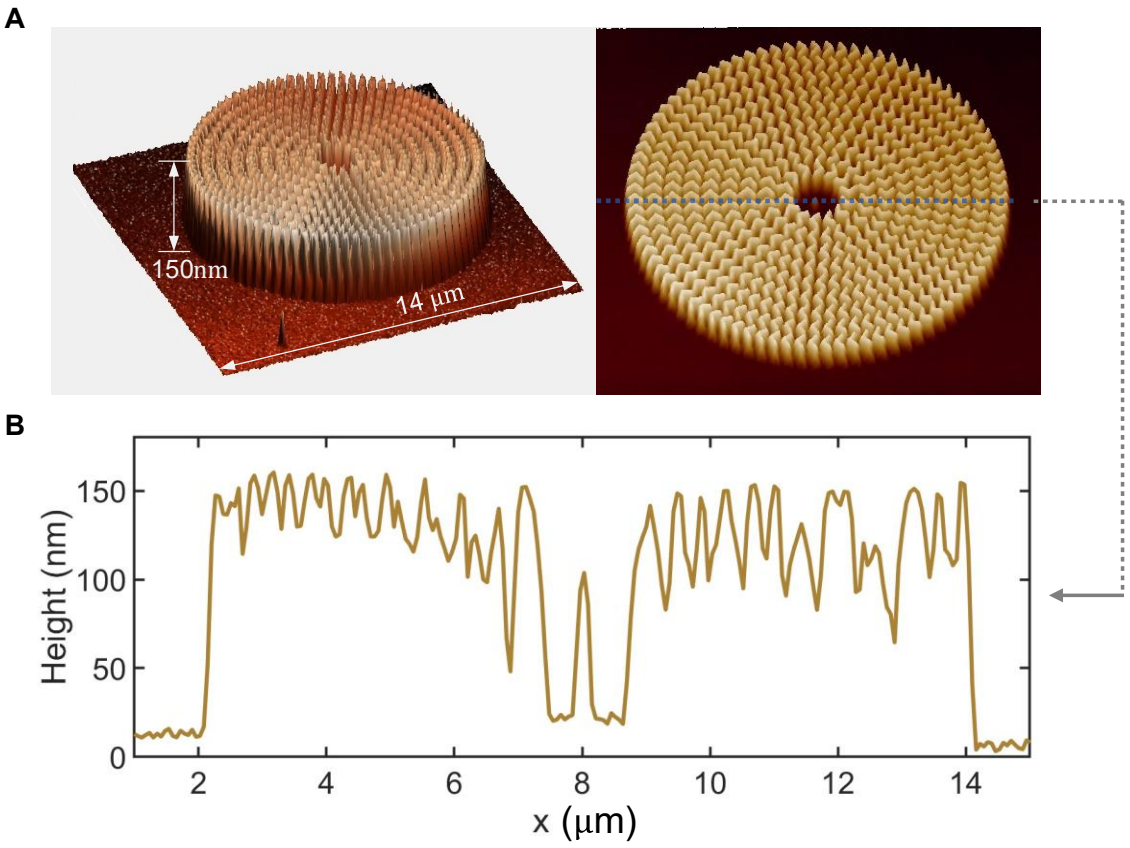

Fig. S11.

AFM of the fabricated devices. (**A**) 3D AFM schematic of the fabricated sample. (**B**) Height of HSQ in the cross section.

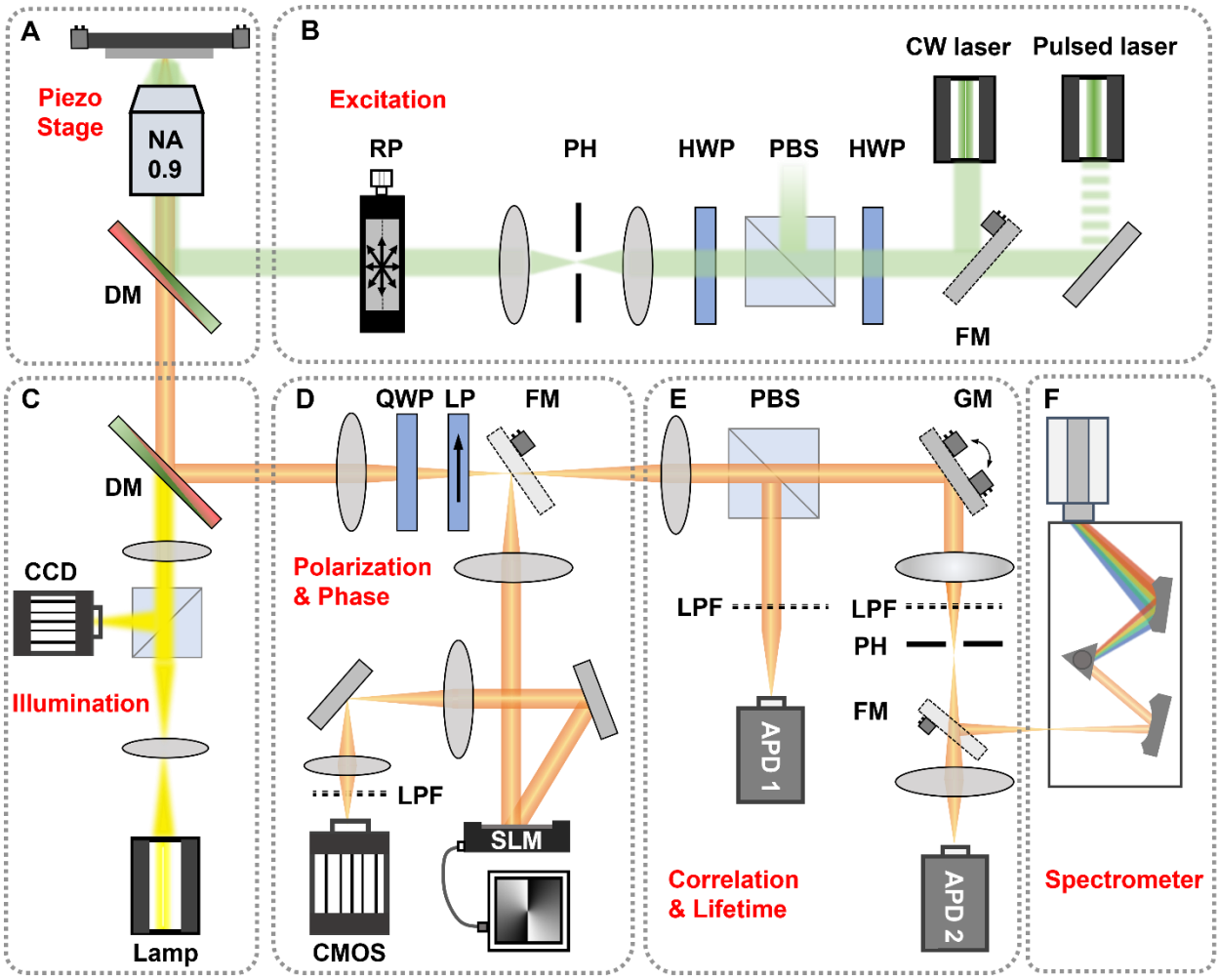

Fig. S12.

Schematic of experimental setup. (**A**) Sample stage. The piezo-stage allows for locating ND-NVs when scanning fluorescence maps. (**B**) Incident light for exciting the nanodiamond. (**C**) Illumination part for finding the fabricated QE-coupled metasurfaces. (**D**) Characterization for polarization states and topological charge. (**E**) Characterization for fluorescence image, correlation, decay-rate. Fluorescence photon rate is recorded by avalanche photo diode (APD1), which is filtered from the laser light, by a set of dichroic mirrors (DM) and a long pass filter (LPF). Correlation measurements is recorded by histogramming the timing delay between photon detection events between APD1 and APD2 in a start-stop configuration, using an electronic timing box (Picharp-300; Pico quant). (**F**) Characterization for spectrum. CW: continuous wave, RP: Radial Polarization Converter, PBS: polarized beam splitter, PH: pinhole, DM: dichroic mirror, LP: linear polarization, QWP: quarter-wave plate, LPF: 550 nm long pass filter, FM: flip mirror, GM: galvanometric mirror. APD: Avalanche Photodiode.

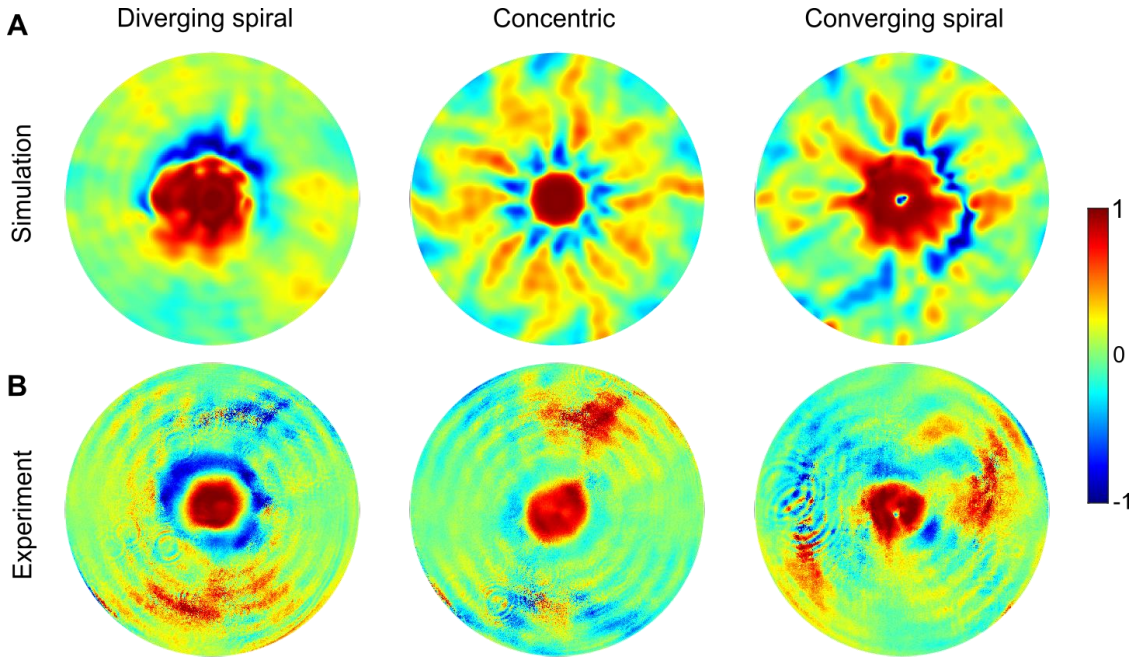

Fig. S13.

Characteristics of the circular polarized states. Simulated (**A**) and measured (**B**) Stokes parameter S_3 distributions of the designed diverging, concentric, and converging configurations.

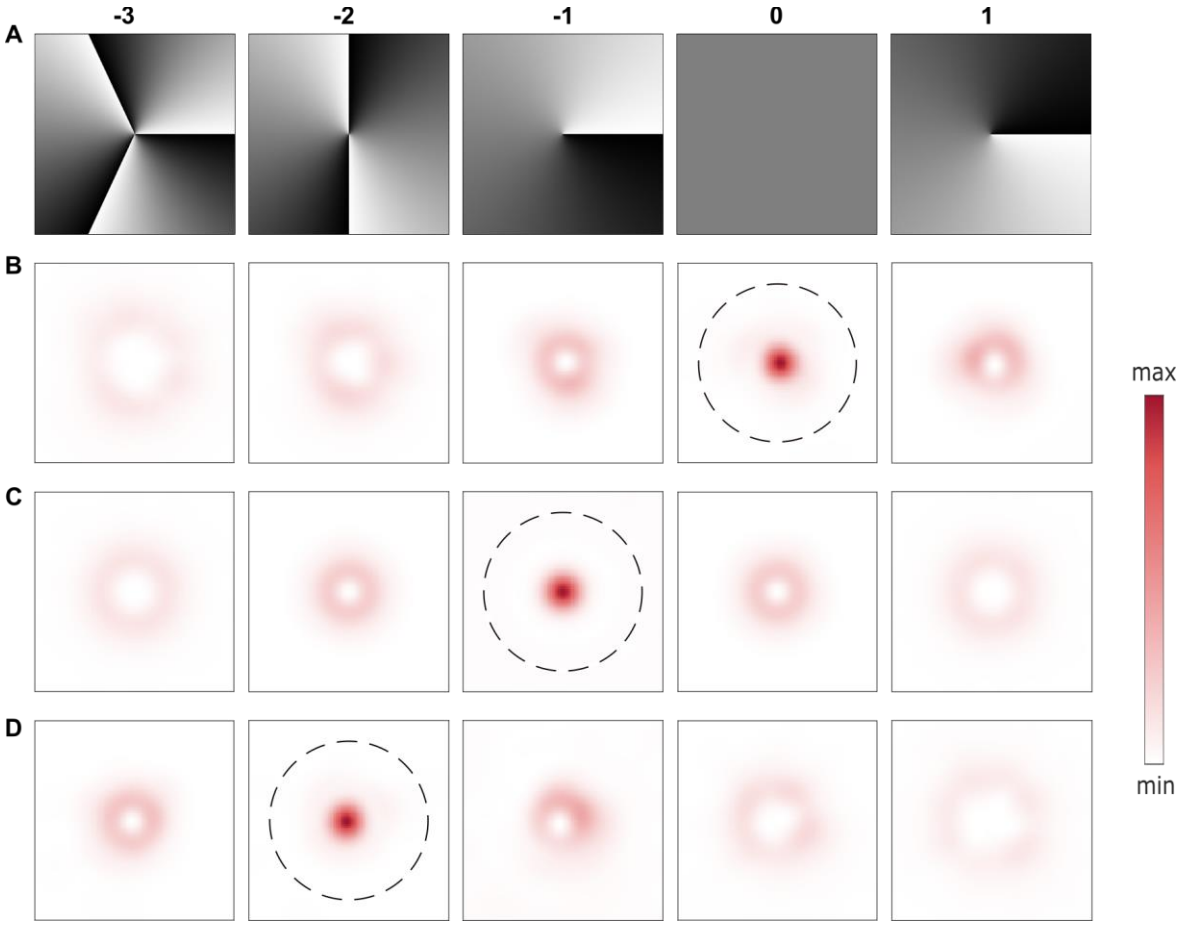

Fig. S14.

Simulated vortex states from QE-couple metasurfaces. (**A**) Phase distribution for holograms with topological charges with -3, -2, -1, 0, and 1. (**B-D**) Simulated intensity distributions of the RCP components of the single-photon emissions that are projected to holograms with (**B**) diverging spiral, (**C**) concentric, (**D**) converging spiral configuration.

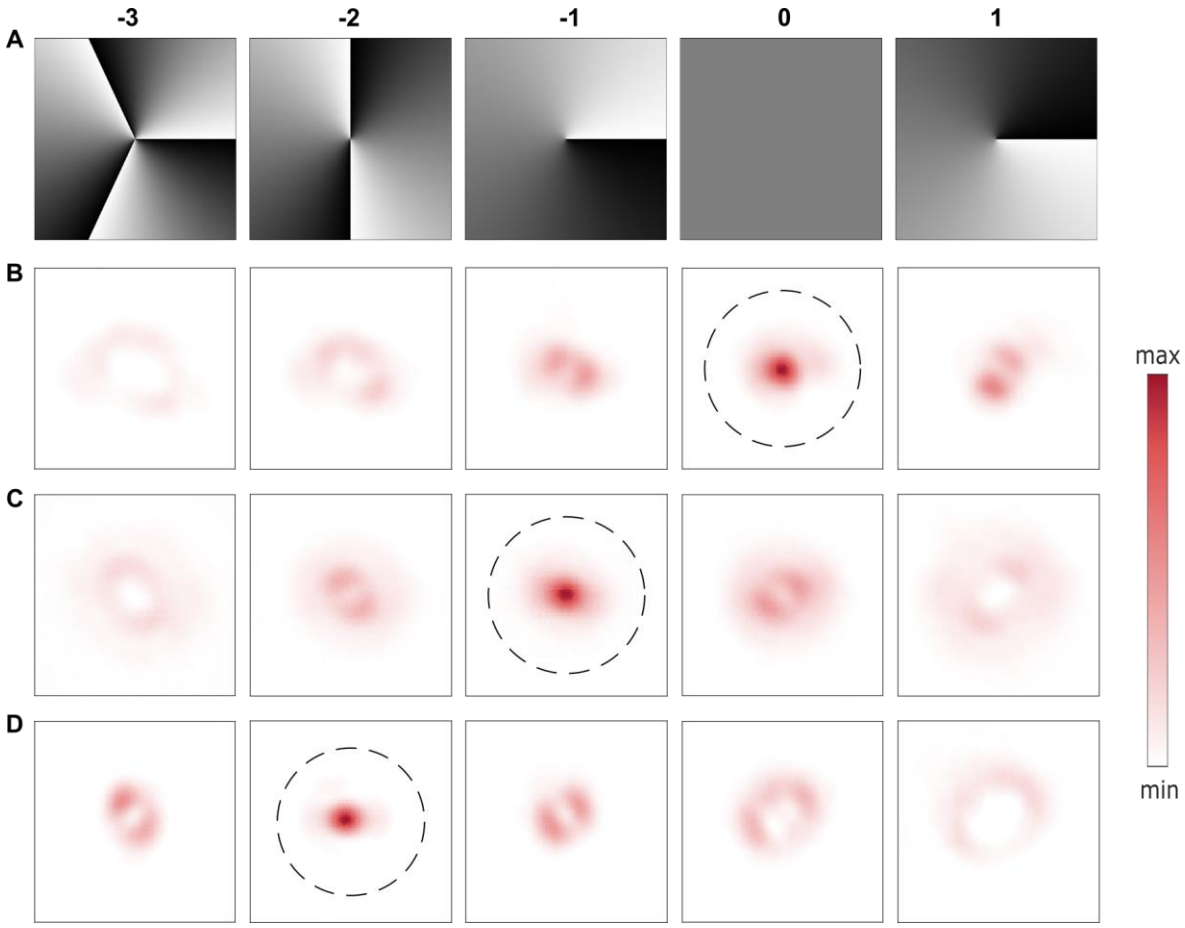

Fig. S15.

Measured vortex states of the designed photon sources with ND-NVs. (**A**) Phase distribution for holograms with topological charges with -3, -2, -1, 0, and 1. (**B-D**) Measured intensity distributions of the RCP components of the single-photon emissions that are projected to holograms with (**B**) diverging spiral, (**C**) concentric, (**D**) converging spiral configuration.

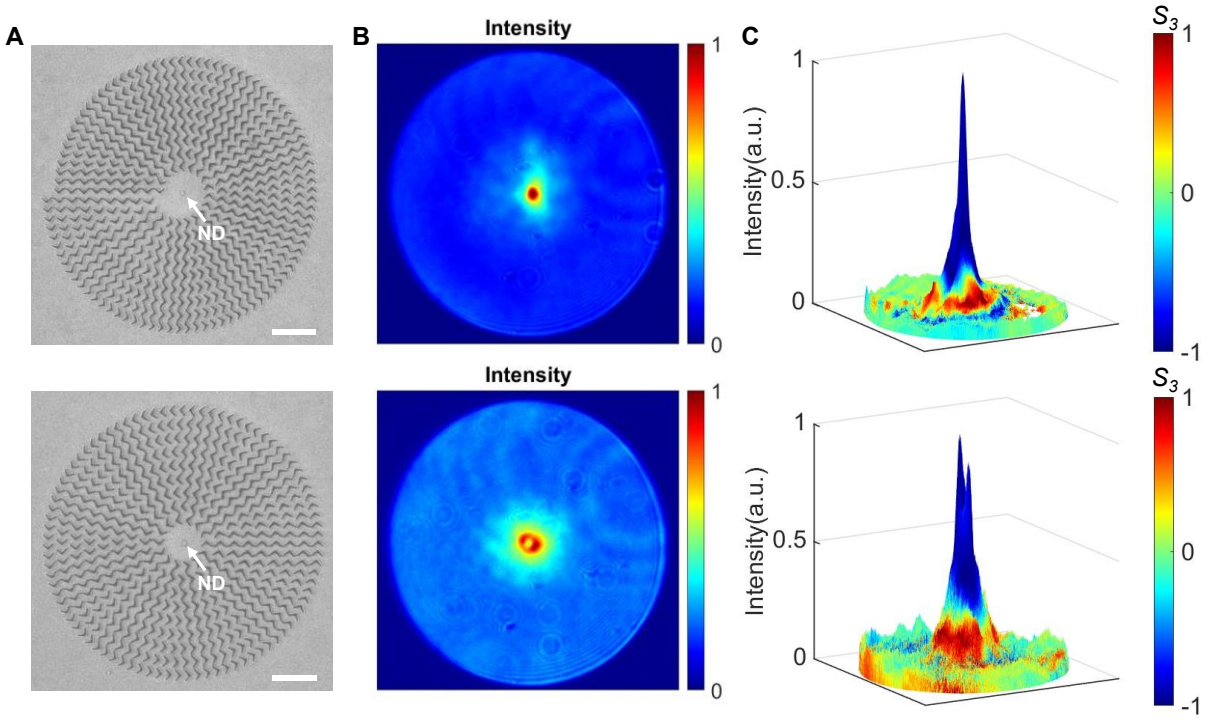

Fig. S16.

Experimental demonstration of left-hand circular polarized (LCP) vortex photon sources. **(A)** SEM images of the fabricated circularly polarized vortex photon sources with topological charge of 0 (top) and 1 (bottom). **(B)** Far-field intensity distribution. **(C)** 3D representation of the superimposed intensity and polarization distribution. The height indicating the intensity and the colour shows the value of Stokes Vector S_3.

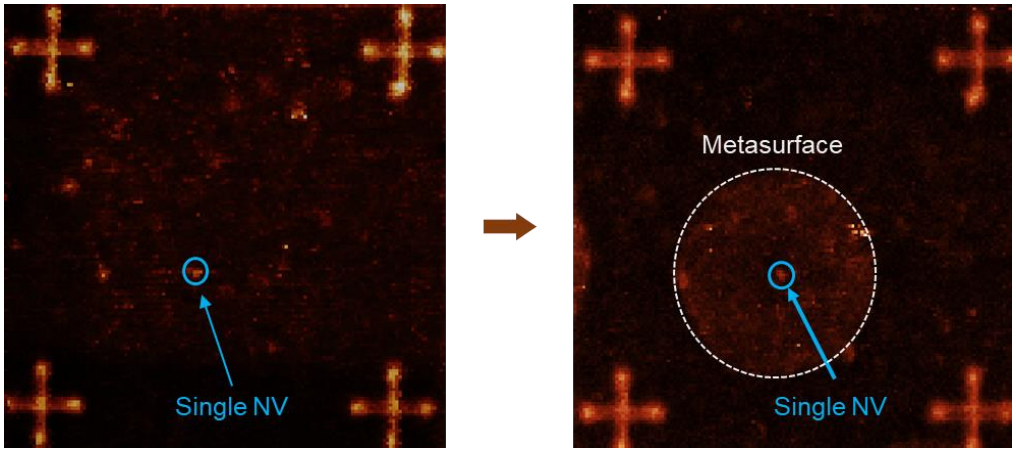

Fig. S17.
Fluorescence image of single-photon source before and after coupling with metasurface.

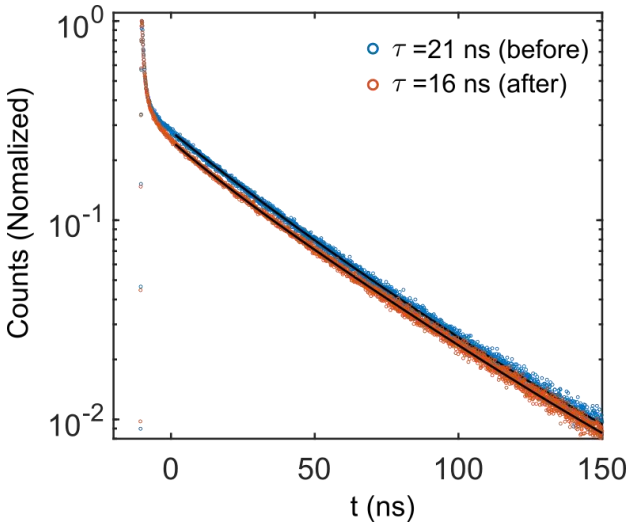

Fig. S18.
Lifetime of single photon sources before and after coupling with metasurfaces.

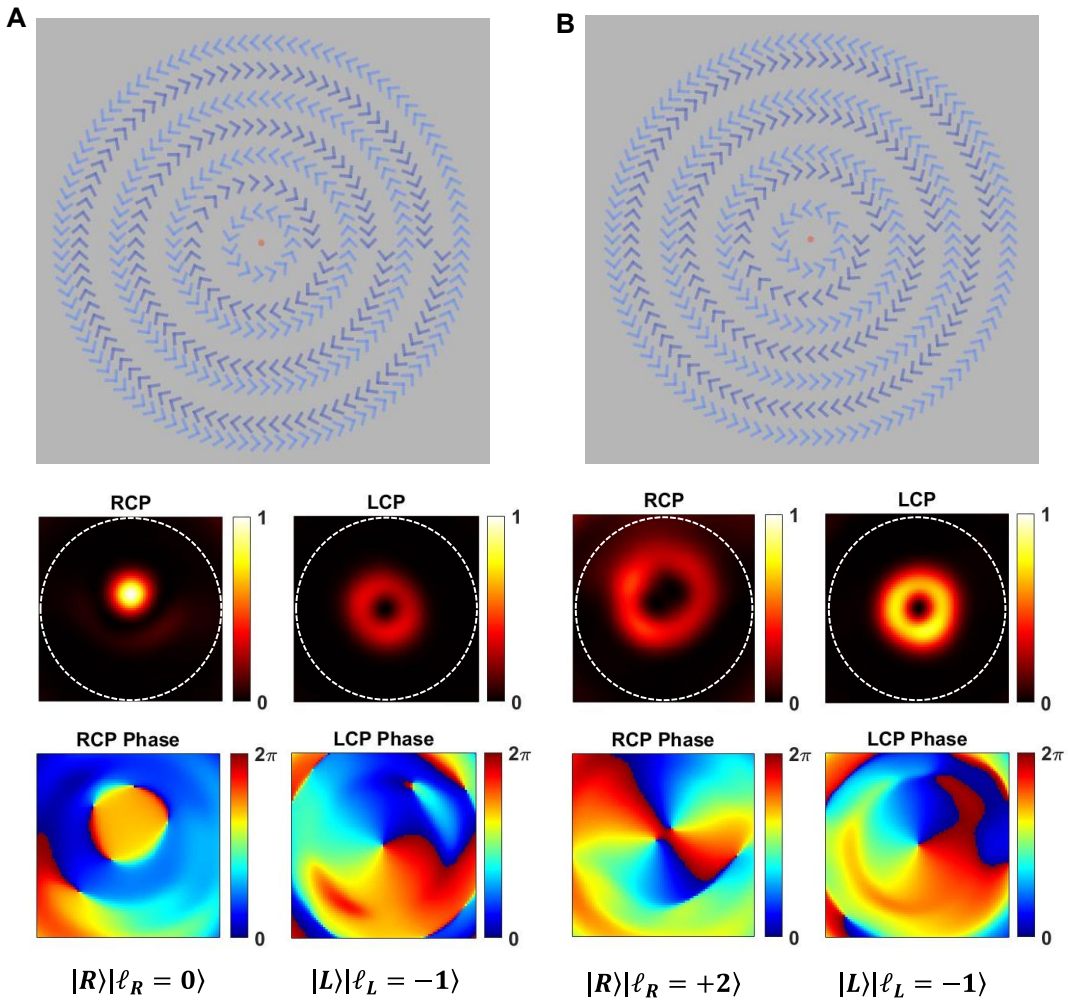

Fig. S19.

Hybrid arrangements of QE-coupled quantum metasurfaces. (**A**) Combination of diverging spiral (RCP element) and concentric (LCP element) for realizing entangled states of $|R\rangle|\ell_R = 0\rangle$ and $|L\rangle|\ell_L = -1\rangle$. (**B**) Combination of converging spiral (RCP element) and concentric (LCP element) for realizing entangled states of $|R\rangle|\ell_R = +2\rangle$ and $|L\rangle|\ell_L = -1\rangle$. The first row is the top view of designed QE-coupled quantum metasurfaces, the second row is the RCP and LCP intensities, the third row is the corresponding phases. Note that all the bricks are made by same dielectric materials (HSQ), the difference of colour in first row just identifies the elements with different orientations that contributes to either RCP or LCP. The white dashed circles denote the numerical aperture NA = 0.2.

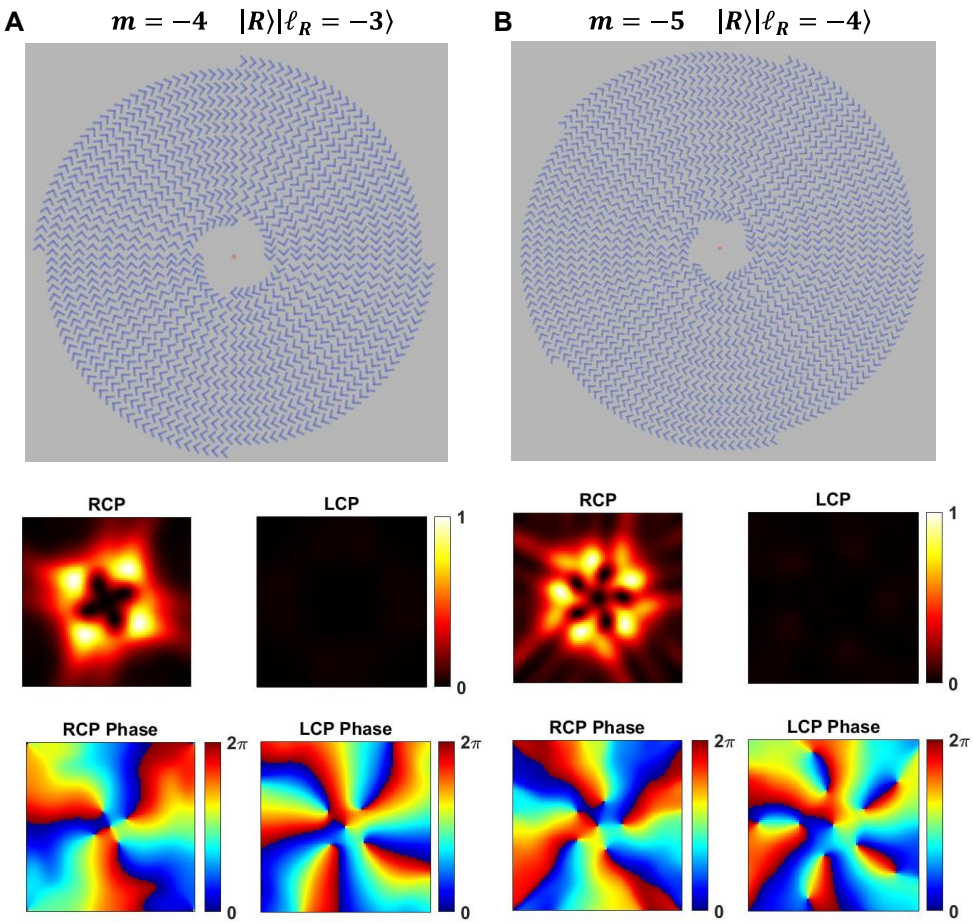

Fig. S20.

High order OAM with different number of spiral arms. (**A**) RCP element arranged with diverging spiral arms ($m = -4$) for realizing states of $|R\rangle|\ell_R = -3\rangle$. (**B**) RCP element arranged with diverging spiral arms ($m = -5$) for realizing states of $|R\rangle|\ell_R = -4\rangle$. m is the number of spiral arms (m < 0 for diverging or m > 0 for converging spirals).

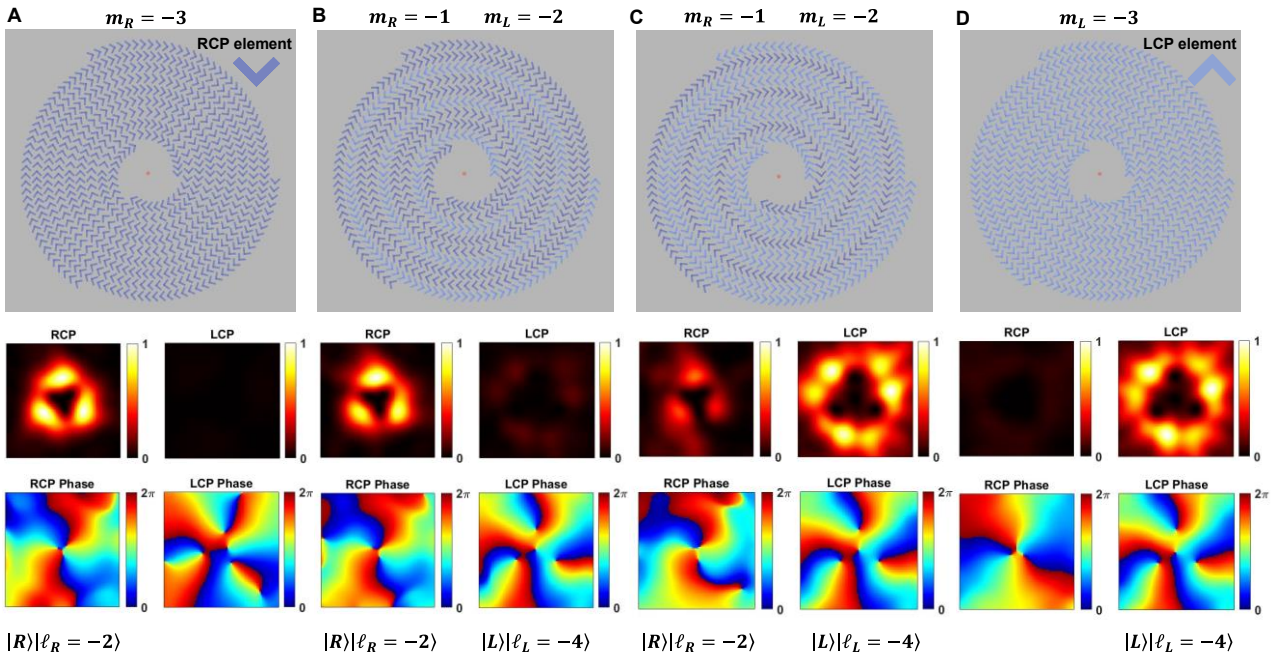

Fig. S21.

Manipulation of SAM and OAM with different chirality of element with a fixed trajectory. (**A**) RCP element arranged with diverging spiral arms ($m = -3$) for realizing states of $|R\rangle|\ell_R = -2\rangle$. (**B**) Combination of RCP element (2 arms) and LCP element (1 arm) for realizing composite states of $|R\rangle|\ell_R = -2\rangle$ and $|L\rangle|\ell_L = -4\rangle$, dominated by $|R\rangle|\ell_R = -2\rangle$. (**C**) Combination of RCP element (1 arm) and LCP element (2 arms) for realizing states of $|R\rangle|\ell_R = -2\rangle$ and $|L\rangle|\ell_L = -4\rangle$, dominated by $|L\rangle|\ell_L = -4\rangle$. (**D**) LCP element arranged with diverging spiral arms ($m = -3$) for realizing states of $|L\rangle|\ell_L = -4\rangle$.

REFERENCES AND NOTES

1. A. Mair, A. Vaziri, G. Weihs, A. Zeilinger, Entanglement of the orbital angular momentum states of photons. *Nature* **412**, 313–316 (2001).

2. G. Molina-Terriza, J. P. Torres, L. Torner, Twisted photons. *Nat. Phys.* **3**, 305 (2007), 310.

3. C. H. Bennett, D. P. DiVincenzo, Quantum information and computation. *Nature* **404**, 247–255 (2000).

4. N. Gisin, R. Thew, Quantum communication. *Nat. Photon.* **1**, 165–171 (2007).

5. X.-L. Wang, X.-D. Cai, Z.-E. Su, M.-C. Chen, D. Wu, L. Li, N.-L. Liu, C.-Y. Lu, J.-W. Pan, Quantum teleportation of multiple degrees of freedom of a single photon. *Nature* **518**, 516–519 (2015).

6. A. Sit, F. Bouchard, R. Fickler, J. Gagnon-Bischoff, H. Larocque, K. Heshami, D. Elser, C. Peuntinger, K. Günthner, B. Heim, C. Marquardt, G. Leuchs, R. W. Boyd, E. Karimi, High-dimensional intracity quantum cryptography with structured photons. *Optica* **4**, 1006–1010 (2017).

7. A. Fleischer, O. Kfir, T. Diskin, P. Sidorenko, O. Cohen, Spin angular momentum and tunable polarization in high-harmonic generation. *Nat. Photonics* **8**, 543–549 (2014).

8. P. Lodahl, S. Mahmoodian, S. Stobbe, A. Rauschenbeutel, P. Schneeweiss, J. Volz, H. Pichler, P. Zoller, Chiral quantum optics. *Nature* **541**, 473–480 (2017).

9. A. Javadi, D. Ding, M. H. Appel, S. Mahmoodian, M. C. Löbl, I. Söllner, R. Schott, C. Papon, T. Pregnolato, S. Stobbe, L. Midolo, T. Schröder, A. D. Wieck, A. Ludwig, R. J. Warburton, P. Lodahl, Spin–photon interface and spin-controlled photon switching in a nanobeam waveguide. *Nat. Nanotechnol.* **13**, 398–403 (2018).

10. J. Wang, J.-Y. Yang, I. M. Fazal, N. Ahmed, Y. Yan, H. Huang, Y. Ren, Y. Yue, S. Dolinar, M. Tur, A. E. Willner, Terabit free-space data transmission employing orbital angular momentum multiplexing. *Nat. Photon.* **6**, 488–496 (2012).

11. N. Bozinovic, Y. Yue, Y. Ren, M. Tur, P. Kristensen, H. Huang, A. E. Willner, S. Ramachandran, Terabit-scale orbital angular momentum mode division multiplexing in fibers. *Science* **340**, 1545–1548 (2013).

12. Z.-Y. Zhou, Y. Li, D.-S. Ding, W. Zhang, S. Shi, B.-S. Shi, G.-C. Guo, Orbital angular momentum photonic quantum interface. *Light Sci. Appl* **5**, e16019 (2016).

13. H. H. Arnaut, G. A. Barbosa, Orbital and intrinsic angular momentum of single photons and entangled pairs of photons generated by parametric down-conversion. *Phys. Rev. Lett.* **85**, 286–289 (2000).

14. X. Chen, X. Lu, S. Dubey, Q. Yao, S. Liu, X. Wang, Q. Xiong, L. Zhang, A. Srivastava, Entanglement of single-photons and chiral phonons in atomically thin WSe_2. *Nat. Phys.* **15**, 221–227 (2019).

15. S. Liu, Y. Lou, J. Jing, Orbital angular momentum multiplexed deterministic all-optical quantum teleportation. *Nat. Commun.* **11**, 3875 (2020).

16. G. Li, A. S. Sheremet, R. Ge, T. C. H. Liew, A. V. Kavokin, Design for a nanoscale single-photon spin splitter for modes with orbital angular momentum. *Phys. Rev. Lett.* **121**, 053901 (2018).

17. D. Braukmann, E. R. Glaser, T. A. Kennedy, M. Bayer, J. Debus, Circularly polarized zero-phonon transitions of vacancies in diamond at high magnetic fields. *Phys. Rev. B* **97**, 195448 (2018).

18. I. Söllner, S. Mahmoodian, S. L. Hansen, L. Midolo, A. Javadi, G. Kiršanskė, T. Pregnolato, H. El-Ella, E. H. Lee, J. D. Song, S. Stobbe, P. Lodahl, Deterministic photon–emitter coupling in chiral photonic circuits. *Nat. Nanotechnol.* **10**, 775–778 (2015).

19. B. Chen, Y. Wei, T. Zhao, S. Liu, R. Su, B. Yao, Y. Yu, J. Liu, X. Wang, Bright solid-state sources for single photons with orbital angular momentum. *Nat. Nanotechnol.* **16**, 302–307 (2021).

20. Y. Ma, H. Zhao, N. Liu, Z. Gao, S. S. Mohajerani, L. Xiao, J. Hone, L. Feng, S. Strauf, On-chip spin-orbit locking of quantum emitters in 2D materials for chiral emission. *Optica* **9**, 953–958 (2022).

21. P. G. Kwiat, K. Mattle, H. Weinfurter, A. Zeilinger, A. V. Sergienko, Y. Shih, New high-intensity source of polarization-entangled photon pairs. *Phys. Rev. Lett.* **75**, 4337–4341 (1995).

22. T. Santia-Cruz, S. D. Gennaro, O. Mitrofanov, S. Addamane, J. Reno, I. Brener, M. V. Chekhova, Resonant metasurfaces for generating complex quantum states. *Science*, **377**, 991–995 (2022).

23. T. Stav, A. Faerman, E. Maguid, D. Oren, V. Kleiner, E. Hasman, M. Segev, Quantum entanglement of the spin and orbital angular momentum of photons using metamaterials. *Science* **361**, 1101–1104 (2018).

24. K. Wang, J. G. Titchener, S. S. Kruk, L. Xu, H.-P. Chung, M. Parry, I. I. Kravchenko, Y.-H. Chen, A. S. Solntsev, Y. S. Kivshar, D. N. Neshev, A. A. Sukhorukov, Quantum metasurface for multiphoton interference and state reconstruction. *Science* **361**, 1104–1108 (2018).

25. W. J. M. Kort-Kamp, A. K. Azad, D. A. R. Dalvit, Space-time quantum metasurfaces. *Phys. Rev. Lett.* **127**, 043603 (2021).

26. N. Yu, F. Capasso, Flat optics with designer metasurfaces. *Nat. Mater.* **13**, 139–150 (2014).

27. N. Meinzer, W. L. Barnes, I. R. Hooper, Plasmonic meta-atoms and metasurfaces. *Nat. Photon.* **8**, 889–898 (2014).

28. A. V. Kildishev, A. Boltasseva, V. M. Shalaev, Planar photonics with metasurfaces. *Science* **339**, 1232009 (2013).

29. C.-W. Qiu, T. Zhang, G. Hu, Y. Kivshar, Quo Vadis, metasurfaces? *Nano Lett.* **21**, 5461–5474 (2021).

30. Y. Ming, Y. Intaravanne, H. Ahmed, M. Kenney, Y. Lu, X. Chen, Creating composite vortex beams with a single geometric metasurface. *Adv.Mater.* **34**, 2109714 (2022).

31. A.H. Dorrah, F. Capasso, Tunable structured light with flat optics. *Science* **376**, eabi6860 (2022).

32. A. S. Solntsev, G. S. Agarwal, Y. S. Kivshar, Metasurfaces for quantum photonics. *Nat. Photonics* **15**, 327–336 (2021).

33. Y. Kan, F. Ding, C. Zhao, S. I. Bozhevolnyi, Directional off-normal photon streaming from hybrid plasmon-emitter coupled metasurfaces. *ACS Photonics* **7**, 1111–1116 (2020).

34. R. Bekenstein, I. Pikovski, H. Pichler, E. Shahmoon, S. F. Yelin, M. D. Lukin, Quantum metasurfaces with atom arrays. *Nat. Phys.* **16**, 676–681 (2020).

35. Y. Kan, S. I. Bozhevolnyi, Molding photon emission with hybrid plasmon-emitter coupled metasurfaces. *Adv. Optical Mater.* **10**, 2102697 (2022).

36. L. Li, Z. Liu, X. Ren, S. Wang, V. C. Su, M. K. Chen, C. H. Chu, H. Y. Kuo, B. Liu, W. Zang, G. Guo, L. Zhang, Z. Wang, S. Zhu, D. P. Tsai, Metalens-array–based high-dimensional and multiphoton quantum source. *Science* **368**, 1487–1490 (2020).

37. Y. Kan, S. K. H. Andersen, F. Ding, S. Kumar, C. Zhao, S. I. Bozhevolnyi, Metasurface-enabled generation of circularly polarized single photons. *Adv. Mater.* **32**, 1907832 (2020).

38. D. Komisar, S. Kumar, Y. Kan, C. Wu, S. I. Bozhevolnyi, Generation of radially polarized single photons with plasmonic bullseye antennas. *ACS Photonics* **8**, 2190–2196 (2021).

39. C. Wu, S. Kumar, Y. Kan, D. Komisar, Z. Wang, S. I. Bozhevolnyi, F. Ding, Room-temperature on-chip orbital angular momentum single-photon sources. *Sci. Adv.* **8**, eabk3075 (2022).

40. J. Ni, C. Huang, L.-M. Zhou, M. Gu, Q. Song, Y. Kivshar, C.-W. Qiu, Multidimensional phase singularities in nanophotonics. *Science* **374**, eabj0039 (2021).

41. A. Pors, M. G. Nielsen, G. D. Valle, M. Willatzen, O. Albrektsen, S. I. Bozhevolnyi, Plasmonic metamaterial wave retarders in reflection by orthogonally oriented detuned electrical dipoles. *Opt. Lett.* **36**, 1626–1628 (2011).

42. A. Pors, S. I. Bozhevolnyi, Efficient and broadband quarter-wave plates by gap-plasmon resonators. *Opt. Express* **21**, 2942–2952 (2013).

43. S. Kumar, C. Wu, D. Komisar, Y. Kan, L. F. Kulikova, V. A. Davydov, V. N. Agafonov, S. I. Bozhevolnyi, Fluorescence enhancement of a single germanium vacancy center in a nanodiamond by a plasmonic Bragg cavity. *J. Chem. Phys.* **154**, 044303 (2021).

44. A. Forbes, M. De Oliveira, M. R. Dennis, Structured light. *Nat. Photonics* **15**, 253–262 (2021).

45. J. Zhu, Y. Chen, Y. Zhang, X. Cai, S. Yu, Spin and orbital angular momentum and their conversion in cylindrical vector vortices. *Opt. Lett.* **39**, 4435–4438 (2014).

46. H. G. Berry, G. Gabrielse, A. E. Livingston, Measurement of the Stokes parameters of light. *Appl. Optics* **16**, 3200–3205 (1977).

47. S. K. H. Andersen, S. Bogdanov, O. Makarova, Y. Xuan, M. Y. Shalaginov, A. Boltasseva, S. I. Bozhevolnyi, V. M. Shalaev, Hybrid plasmonic bullseye antennas for efficient photon collection. *ACS Photonics* **5**, 692–698, (2018).

48. H. Wang, Y. M. He, T. H. Chung, H. Hu, Y. Yu, S. Chen, X. Ding, M. C. Chen, J. Qin, X. Yang, R. Z. Liu, Z. C. Duan, J. P. Li, S. Gerhardt, K. Winkler, J. Jurkat, L. J. Wang, N. Gregersen, Y. H. Huo, Q. Dai, S. Yu, S. Höfling, C. Y. Lu, J. W. Pan, Towards optimal single-photon sources from polarized microcavities. *Nat. Photonics* **13**, 770–775 (2019).

49. J. Liu, R. Su, Y. Wei, B. Yao, S. F. C. da Silva, Y. Yu, J. Iles-Smith, K. Srinivasan, A. Rastelli, J. Li, X. Wang, A solid-state source of strongly entangled photon pairs with high brightness and indistinguishability. *Nat. Nanotechnol.* **14**, 586–593 (2019).

50. H. Wang, H. Hu, T. H. Chung, J. Qin, X. Yang, J. P. Li, R. Z. Liu, H. S. Zhong, Y. M. He, X. Ding, Y. H. Deng, Q. Dai, Y. H. Huo, S. Höfling, C. Y. Lu, J. W. Pan, On-demand semiconductor source of entangled photons which simultaneously has high fidelity, efficiency, and indistinguishability. *Phys. Rev. Lett.* **122**, 113602 (2019).

51. A. Pors, M. G. Nielsen, S. I. Bozhevolnyi, Plasmonic metagratings for simultaneous determination of Stokes parameters. *Optica* **2**, 716–723, (2015).

52. A. Yariv, P. Yeh, *Optical Waves in Crystals* (Wiley, 1984), vol. 5.